

Chirality Induced Propagation Velocity Asymmetry

Diego A. Hoff

Universidade Federal da Fronteira Sul, SC, Brazil

Luis G. C. Rego

Department of Physics, Universidade Federal de Santa Catarina, SC, 88040-900, Brazil

Abstract

The spin-dependent propagation of electrons in helical nanowires is investigated. We show that the interplay of spin angular momentum and nanowire chirality, under spin-orbit interaction, lifts the symmetry between left and right propagating electrons, giving rise to a velocity asymmetry. The study is based on a microscopic tight-binding model that takes into account the spin-orbit interaction. The continuity equation for the spin-dependent probability density is derived, including the spin non-conserving terms, and quantum dynamics calculations are performed to obtain the electron propagating dynamics. The calculations are applied to the inorganic double-helix SnIP, a quasi-1D material that constitutes a semiconductor with a band gap of ~ 1.9 eV. The results, nevertheless, have general validity due to symmetry considerations. The relation of the propagation velocity asymmetry with the phenomena ascribed to the chiral-induced spin selectivity (CISS) effect is examined.

Geometrical chirality is easily noticed for a figure whose image in a plane mirror cannot be brought to coincidence with itself. However, this definition is limited because it does not include the broader notion of dynamic chirality, which is more elusive and has far more reaching consequences.^{1,2} The chiral properties of quasi-1D systems have been known from some time. The first systematic study of quantum chiral properties occurred in the 1980's, with the discovery of the Integer Quantum Hall effect – and later the Fractional effect – and the explanation thereof in terms of chiral edge states.³ More recently, quantum chiral properties have been investigated in single wall carbon nanotubes (SWCNT),^{4–8} which can exhibit chiral phenomena depending on their wrapping configuration.⁹ Interestingly, the oldest, most ubiquitous and well known chiral quasi-1D material occurs naturally, the DNA.¹⁰ Nevertheless, until very recently, its quantum chiral properties have gone unnoticed. In a recent experiment, researchers observed that a double-stranded DNA (dsDNA) could generate a spin-polarized electronic current out of a spin-unpolarized electron influx.^{11,12} The effect was named chiral induced spin selectivity (CISS).¹³ From this initial observation various other manifestations of the CISS effect were reported, in a broad range of situations, including separation of chiral enantiomers,¹⁴ spin-filtering,^{15,16} chiral induced spin-LED devices fabricated with layered perovskites,¹⁷ and improved electrocatalytic water splitting with chiral metal-oxide films.^{18,19} Despite the various experimental reports, the fundamental understanding of the effect is still incomplete. Besides the nature of the CISS effect, its surprising robustness in face of the smallness of the spin-orbit interaction in organic materials, even at ambient conditions, constitutes one of the main challenging questions. In fact, several studies have reproduced qualitatively the spin filtering effects observed experimentally, but the calculations generally describe a much weaker effect.^{20–25} Most of the theoretical work is based on the stationary Landauer-Büttiker transport formalism,^{20,21,23,24,26,27} some studies place emphasis on the role played by the contact leads,^{23,28,29} while others report that scattering, decoherence and/or leakage processes are necessary to describe the magnitude of the effect.^{21,22,29–31} Varela et al.²⁷ reported that by considering the sequential tunneling between well defined localized states large spin polarization could be attained with realistic spin-orbit coupling parameters.

In this letter we study the spin-dependent propagation of electrons in helical nanowires. We show that the symmetry of left- and right-propagating electrons is broken due to the spin spin-orbit interaction, so that the mobility of electrons in structures with axial chirality

depends on the combination of 3 factors: the direction of the spin angular momentum, the direction of motion, and the chirality of the underlying physical structure. The study was performed in the totally inorganic SnIP double-helix system.^{32,33} We argue that the propagation velocity asymmetry can be one of the underlying effects responsible for the CISS effect. We also point out that the propagation velocity asymmetry is also described in carbon nanotubes⁸ and chiral metamaterials,³⁴ thus, putting the CISS effect on a common ground with other phenomena.

Model system. We briefly describe the characteristics of the tin iodide phosphide (SnIP) double-helix,^{32,33} shown in Figure 1, which has a totally inorganic double-helical structure. The SnIP double-helix consists of an inner $[P]^-$ (phosphorus) helix wrapped by an outer $[SnI]^+$ (tin iodide) helix, giving rise to a non-magnetic double-helix of 0.98 nm in outer diameter. We call attention to the fact that both the inner $[P]^-$ and the outer $[SnI]^+$ helices comprising a given SnIP double-helix have the same chirality; here the plus and minus signs designate the oxidation states. Each nanorod is held together by strong intra-helix covalent bonds and a dative ionic interaction between the inner and outer helices. As synthesized, the nanorods are assembled in bundles by van der Waals forces, giving rise to a semiconductor material that exhibits quasi-1D quantum confinement effects. The bundles consist of a racemic mixture of left-handed and right-handed double-helices aligned parallel to each other in a pseudo-hexagonal arrangement. Material characterization shows that the SnIP double-helices constitute a material with an indirect band gap of 1.80 eV and a direct band gap of 1.86 eV.³² In addition, the material is highly flexible and stable, showing polymer like behavior.³³ Time-resolved terahertz (THz) spectroscopy revealed a high intrinsic electron mobility along the double-helix axis, which is limited by traps.³⁵ Individual SnIP double-helix strands can be obtained from the racemic mixture by minimizing the van de Waals force and stabilizing the single strands in a different medium, such as in SnIP@C₃N₄(F,Cl) thin films.³³ Another possibility, as indicated by total energy calculations,^{33,36} is the encapsulation of individual strands in carbon nanotubes. Herein, we use the geometrical parameters obtained in reference³² to build the unit cell of the model system. Within the helices, bond distances vary as: $d(Sn-I) = 3.060$ to 3.288 Å, for the outer tin-iodide helix, and $d(P-P) = 2.17$ to 2.21 Å for the inner phosphorus helix. Seven SnIP units comprise the double-helix unit cell, with a lattice parameter of $a = 7.934$ Å. Figure 1 shows a 3 unit cell left-handed strand.

Theory and Methods. The single particle hamiltonian of an electron in the double-

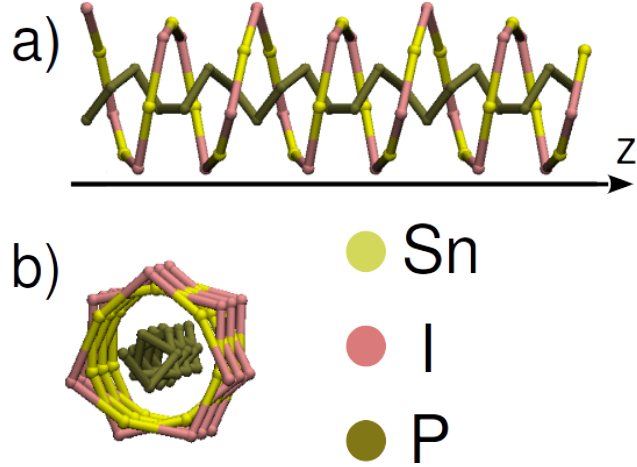


FIG. 1. Geometrical structure of a left-handed M-SnIP double-helix comprised of 3 unit cells: a) aligned along the z axis and b) frontal viewpoint. Notice that both the inner $[\text{P}]^-$ and the outer $[\text{SnI}]^+$ helices have the same left-handed M-chirality; the plus and minus signs designate the oxidation states.

helical SnIP nanowire, including the spin-orbit interaction term, is given by

$$H = \frac{1}{2m}\mathbf{p}^2 + V(\mathbf{r}) + \frac{1}{2(mc)^2}\mathbf{S} \cdot \nabla V(\mathbf{r}) \times \mathbf{p}, \quad (1)$$

where $\mathbf{S} = \frac{\hbar}{2}\boldsymbol{\sigma} = \frac{\hbar}{2}(\sigma_x, \sigma_y, \sigma_z)$ is the spin vector operator comprised of the σ Pauli matrices, $\mathbf{p} = -i\hbar\nabla$ is the electron momentum operator and $V(\mathbf{r})$ is the total Coulomb potential energy felt by the electron. We make use of the tight-binding (TB) formalism. Several studies have used the TB method, either in the Slater-Koster^{7,21,23,37} (SK) or the extended-Hückel^{38,39} (eH) framework, to describe carbon nanotubes and DNA molecules. Herein, we adopt the eH approach. The total hamiltonian, Eq. (1), is comprised of a spinless part (H_0), associated with the eH-TB hamiltonian, and the spin-orbit interaction part. We compute the TB hamiltonian in the basis of atomic Slater-type orbitals (STO's), $|\chi_{nlm}s\rangle$, where $i = \{nlm\}$ represents the orbital quantum numbers associated with the wavefunction $\chi_{nlm}(\mathbf{r}_\alpha) = \mathcal{R}_n(r_\alpha)Y_{lm}(\theta, \varphi)$, and $s = \{-1, 1\}$ (lowercase s) designates the spin state of the electron along the z direction. The wavefunction components $\mathcal{R}_n(r_\alpha)$ and $Y_{lm}(\theta, \varphi)$ describe, respectively, the radial and the angular parts of the STO for an atom located at position \mathbf{R}_α , with $\mathbf{r}_\alpha = \mathbf{r} - \mathbf{R}_\alpha$. The basis set includes the 3s and 3p atomic orbitals for the phosphorus (P) atoms and the 5s and 5p orbitals for the tin (Sn) and iodine (I) atoms. The matrix elements of the spinless semiempirical eH hamiltonian are provided as Supporting Information. The

spin-orbit (SO) interaction part

$$H_{SO} = \frac{1}{2(mc)^2} \mathbf{S} \cdot \nabla V(\mathbf{r}) \times \mathbf{p} \quad (2)$$

is also written in the framework of the eH-TB formalism.³⁹ Despite the complexity of the SO term, the main contribution of the SO interaction arises from the one-electron operators that couple the electron with the nuclei.⁴⁰ Therefore, in the TB method, the total Coulomb potential can be approximated by a summation over spherically symmetric single particle potentials produced by all the nuclei α , $V(\mathbf{r}) \approx \sum_{\alpha} V_{\alpha}(|\mathbf{r} - \mathbf{R}_{\alpha}|)$, so that

$$H_{SO} \approx \sum_{\alpha} \frac{1}{2m^2c^2} \frac{1}{|\mathbf{r}_{\alpha}|} \frac{dV_{\alpha}(r_{\alpha})}{dr_{\alpha}} \mathbf{S} \cdot \mathbf{L}_{\alpha} = \sum_{\alpha} \hat{\lambda}_{\alpha}(r_{\alpha}) \frac{\mathbf{S} \cdot \mathbf{L}_{\alpha}}{\hbar^2}, \quad (3)$$

with $\mathbf{L}_{\alpha} = (\mathbf{r} - \mathbf{R}_{\alpha}) \times \mathbf{p}$ describing the angular momentum of the electron with respect to atom α . It has been shown that the effective single particle SO operator $\xi_{\alpha} \mathbf{S} \cdot \mathbf{L}_{\alpha}$ produces very good results⁴⁰ when the coupling parameter ξ_{α} is obtained from ab-initio calculations or experimental fits, so as to incorporate SO many-body effects.

The matrix elements of H_{SO} can be written as

$$\langle is_i, \beta | H_{SO} | js_j, \gamma \rangle = \sum_{\alpha} \langle is_i, \beta | \left(\hat{\lambda}_{\alpha}(r_{\alpha}) \frac{\mathbf{S} \cdot \mathbf{L}_{\alpha}}{\hbar^2} \right) | js_j, \gamma \rangle, \quad (4)$$

with β and γ designating the atoms located at positions \mathbf{R}_{β} and \mathbf{R}_{γ} . The matrix element of Eq. (S4) renders *intra* and *inter*-atomic terms. Among them, the one-center *intra*-atomic terms ($\alpha = \beta = \gamma$) have overwhelming weight, followed by the two-center terms, for which two of the atomic site indices are equal, that account for 2% to 5% of the SO splitting.⁴⁰ The three-center terms ($\alpha \neq \beta \neq \gamma$) are, thus, disregarded altogether. Due to the spherical symmetry, the *intra*-atomic matrix elements centered in an arbitrary atom α can be factored as

$$\langle is_i | H_{SO}^{intra} | js_j \rangle_{\alpha} = \langle \mathcal{R}(r_{\alpha}) | \hat{\lambda}_{\alpha}(r_{\alpha}) | \mathcal{R}(r_{\alpha}) \rangle \langle l_i m_i s_i, \alpha | \frac{\mathbf{S} \cdot \mathbf{L}_{\alpha}}{\hbar^2} | l_j m_j s_j, \alpha \rangle, \quad (5)$$

where the radial part can be associated with the empirical λ_{α}^{SOC} parameter

$$\langle \mathcal{R}(r_{\alpha}) | \frac{\hbar^2}{2m^2c^2} \frac{1}{r_{\alpha}} \frac{dV_{\alpha}(r_{\alpha})}{dr_{\alpha}} | \mathcal{R}(r_{\alpha}) \rangle = \lambda_{\alpha}^{SOC}. \quad (6)$$

We obtain the SOC constants λ_{α}^{SOC} (Table S2) from the literature for the P, Sn and I elements.

Having defined the *intra*-atomic matrix elements, the *inter*-atomic ones can be obtained thereof (see Supporting Information), by using the Mulliken approximation for multicenter integrals.⁴¹ Therefore, we write the expression for the matrix elements of the spin-orbit coupling in the eH-TB framework as³⁹

$$\langle is_i, \beta | H_{SO} | js_j, \gamma \rangle = \delta_{\beta, \gamma} \sum_{\alpha} \sum_{k, l \in \alpha} S_{ik}(\beta, \alpha) S_{lj}(\alpha, \beta) \langle ks_k | H_{SO}^{intra} | ls_l \rangle_{\alpha} + (1 - \delta_{\beta, \gamma}) \left\{ \sum_{k \in \beta} S_{kj}(\beta, \gamma) \langle is_i | H_{SO}^{intra} | ks_k \rangle_{\beta} + \sum_{k \in \gamma} S_{ik}(\beta, \gamma) \langle ks_k | H_{SO}^{intra} | js_j \rangle_{\gamma} \right\}, \quad (7)$$

The overlap matrix is block diagonal in the spinor Hilbert space. The SO interaction is considered on the same level as the H_0 hamiltonian.

Once we have the total hamiltonian $H = H_0 + H_{SO}$, the generalized eigenvalue equation $H\Phi = S\Phi E_{diag}$ is solved to yield the molecular orbitals of the entire double-helix in the form of eigenpairs (ϵ_n, Φ_n) , written as spinors in the basis of the atomic STO's

$$\Phi_n(\mathbf{r}) = \sum_{\nu, s=\uparrow, \downarrow} A_{\nu s}^n \chi_{\nu s}(\mathbf{r}), \quad (8)$$

where the combined index ν designates the pair of indices (i, α) . Due to the spin degree of freedom, both H_0 and S are block diagonal matrices, with each block associated with a different spin projection of the spinor. To calculate the electron propagation in the SnIP double-helix, we solve the time-dependent Schrödinger equation (TDSE) for an arbitrary initial quantum state $|\Psi\rangle$

$$i\hbar \frac{\partial}{\partial t} |\Psi(t)\rangle = (\hat{H}_0 + \hat{H}_{SO}) |\Psi(t)\rangle, \quad (9)$$

disregarding the nuclear motion. We write the arbitrary quantum state in terms of the energy eigenstates, as $\Psi(\mathbf{r}) = \sum_n C_n \Phi_n(\mathbf{r})$. Thus, the time evolution of Ψ is given by

$$\Psi(\mathbf{r}, t) = e^{-i\hat{H}t/\hbar} \Psi(\mathbf{r}) = \sum_n e^{-i\epsilon_n t/\hbar} C_n \Phi_n(\mathbf{r}, 0). \quad (10)$$

In order to get information about the spatial distribution of $\Psi(\mathbf{r}, t)$ as well as its spin probability density we use Eq. (8), so that

$$\Psi(\mathbf{r}, t) = \sum_n e^{-i\epsilon_n t/\hbar} C_n \sum_{\nu s} A_{\nu s}^n \chi_{\nu s}(\mathbf{r}) = \sum_{\nu s} Q_{\nu s}(t) \chi_{\nu s}(\mathbf{r}), \quad (11)$$

where $Q_{\nu s}(t) = \sum_n \exp[-i\epsilon_n t/\hbar] C_n A_{\nu s}^n$, with ν designating the orbital quantum numbers and $s = \uparrow, \downarrow$ for the spin projection along the z direction. For convenience, we separate the wavefunction according to their spin components as

$$\Psi(\mathbf{r}, t) = \sum_s \Psi_s(\mathbf{r}, t) = \sum_{\nu} \{Q_{\nu\uparrow}(t)\chi_{\nu\uparrow}(\mathbf{r}) + Q_{\nu\downarrow}(t)\chi_{\nu\downarrow}(\mathbf{r})\}. \quad (12)$$

Spin probability current.

It has been pointed out that the conventional spin current, usually defined as $\mathbf{j}_s = \frac{\hbar}{m} \Im m [\Psi_s^* \nabla \Psi_s]$, or alternatively as the mean value of the operator $(1/2)(\hat{\mathbf{v}} \hat{\mathbf{S}} + \hat{\mathbf{S}} \hat{\mathbf{v}})$, is incomplete and unphysical under spin-flip hamiltonians.⁴²⁻⁴⁵ Thus, by considering the spin-orbit interaction, the continuity equation for the probability density is written as

$$\begin{aligned} \sum_{s=\uparrow,\downarrow} \frac{\partial |\Psi_s|^2}{\partial t} = & -\nabla \cdot \left\{ \frac{\hbar}{m^*} \sum_{s=\uparrow,\downarrow} \Im m [\Psi_s^* \nabla \Psi_s] \right\} \\ & - \nabla \cdot \left\{ \frac{1}{2(m^*c)^2} \sum_{s,s'} [\Psi_s^* \mathbf{S}_{s,s'} \Psi_{s'}] \times \nabla V(\mathbf{r}) \right\}, \end{aligned} \quad (13)$$

where we have omitted the time variable for the sake of clarity (details provided as Supporting Information). The LHS is simply the time-dependent total probability density whereas, on the RHS, we identify the conventional probability density current of well defined spin channel, $\mathbf{j}_s = \frac{\hbar}{m^*} \Im m [\Psi_s^* \nabla \Psi_s]$, and the spin-mixed probability density current that is due to the spin-orbit interaction,

$$\sum_{s'} \mathbf{j}_{s,s'}^{SO} = \sum_{s'} \frac{1}{2(m^*c)^2} [\Psi_s^* \mathbf{S}_{s,s'} \Psi_{s'}] \times \nabla V(\mathbf{r}). \quad (14)$$

The later has also been associated with the torque dipole density⁴² or the angular spin current density.⁴³ The effective mass m^* is a consequence of the tight-binding formalism. Equation (13) essentially connects the quantum dynamics, on the LHS, with the measurable current densities on the RHS. It can be written in terms of the probability current densities as

$$\sum_{s=\uparrow,\downarrow} \frac{\partial \rho_s}{\partial t} = -\nabla \cdot \sum_s \left\{ \mathbf{j}_s + \sum_{s'} \mathbf{j}_{s,s'}^{SO} \right\}. \quad (15)$$

To calculate the electronic transport in the double helix we integrate the continuity equation over a volume \mathcal{V} along the nanowire axis (Figure S1) and apply the divergence theorem to obtain

$$\frac{\partial}{\partial t} [P_{\uparrow} + P_{\downarrow}]_{\mathcal{V}} = - \sum_s \int_{\mathcal{S}} j_{z,s} dA_{\perp} - \int_{\mathcal{S}} \left[\sum_{s,s'} j_{s,s'}^{SO} \right]_z dA_{\perp}, \quad (16)$$

where P_s is the spin-dependent electron population inside \mathcal{V} , associated with the spinor wavepackets $\Psi_s(\mathbf{r}, t)$. On the RHS, $j_{z,s}dA_\perp$ is the probability density flux with well defined spin projection across the surface caps perpendicular to the \hat{z} direction. The last term accounts for the probability density flux of the mixed-spin current. At this point, we can write down an expression for the mixed-spin current (see Supporting Information). In order to have consistency between the TB matrix element of Eq. (S6) and the spin-orbit hamiltonian of Eq. (S2) we assume that the SOC constant is given by a Coulomb potential that is generated by an effective charge Q'_α , for each of the atomic species in the double-helix.

That is

$$\nabla V(\mathbf{r}) \approx \sum_\alpha \nabla V_\alpha(\mathbf{r} - \mathbf{R}_\alpha) \approx \sum_\alpha \frac{-e}{r_\alpha} \frac{d}{dr_\alpha} \left(\frac{Q'_\alpha}{r_\alpha} \right) \mathbf{r}_\alpha . \quad (17)$$

Then, we substitute Eq. (17) into Eq. (6), which is integrated over the radial part of the STO's to yield the effective charges in terms of the SOC constants (Table S2) that are obtained from the literature. As a result, we obtain a spin-orbit interaction operator that is consistent with the eH-TB formalism. Thus, the mixed-spin current flux along the axis of the double-helix can be explicitly written as

$$\left[\sum_{s,s'} j_{s,s'}^{SO} \right]_z \approx \frac{\hbar}{2(m^*c)^2} \left(\Im m(\Psi_\downarrow^* \Psi_\uparrow) \sum_\alpha \frac{Q'_\alpha x_\alpha}{r_\alpha^3} - \Re e(\Psi_\downarrow^* \Psi_\uparrow) \sum_\alpha \frac{Q'_\alpha y_\alpha}{r_\alpha^3} \right) , \quad (18)$$

with $\Psi_s(\mathbf{r}, t)$ given by Eq. (11).

Spin dependent electron transport. Let us consider a long strand of the SnIP double-helix, either of M (left-handed) or P (right-handed) chirality, subject to periodic boundary conditions, so that it is topologically equivalent to a double-helix ring, without deforming its original geometric structure. Figure 2 illustrates the concept. Herein, for purposes of calculations, we assume an M-SnIP double-helix composed of 97 unit cells. We consider that the initial wavepacket $\Psi(\mathbf{r}, t = 0)$ is created in a small portion of the strand, denominated source (S), which is comprised of 3 SnIP unit cells, as depicted in green in Figure 2-b. In practice the source segment could be associated with an electrode, or a scanning tunneling microscope (STM) tip that injects electrons in the double-helix. Since the initial wavepacket $\Psi(\mathbf{r}, t = 0)$ is not a stationary state of the entire strand, by solving the TDSE we observe that it splits in two symmetrical wavepackets that propagate in opposite directions. After a "time-of-flight" both travelling wavepackets are detected in the detector segment (D), which is equally distant from S by clockwise (CW) or counter-clockwise (CCW) paths. The

detector segment is comprised of 4 SnIP unit cells, as depicted in red in Figure 2-b. The detection of the travelling wavepackets in D is calculated with the continuity equation, Eq. (S33). From the experimental point of view, the electron detection could be accomplished by electric contacts or luminescent probes. The same calculations were also performed on P-SnIP double-helices (see Supporting Information).

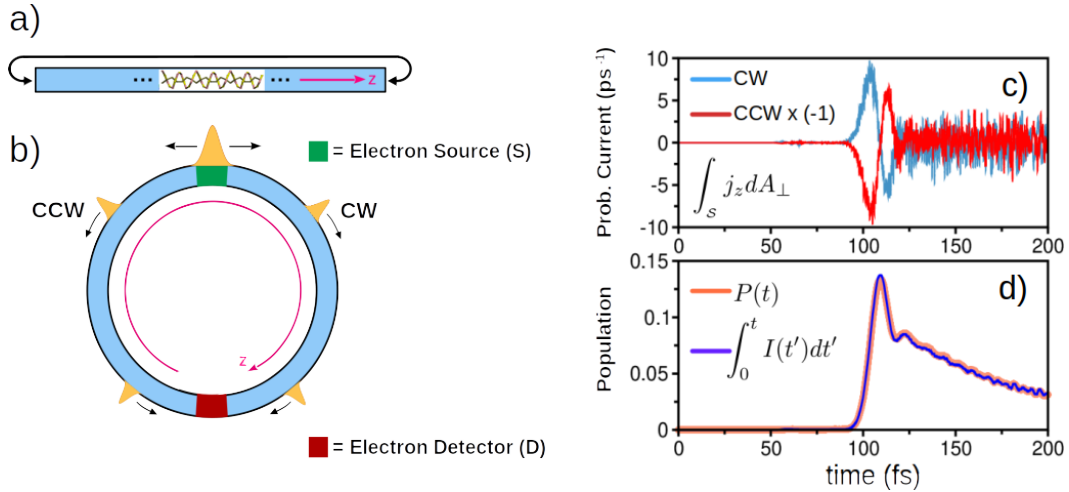


FIG. 2. a) SnIP double-helix oriented along the \hat{z} direction with periodic boundary conditions. b) The SnIP periodic structure is topologically equivalent to a ring. The green segment designates the electron source (S), where $\Psi(\mathbf{r}, t = 0)$ is created (or injected). The red segment designates the drain, where the electron is detected (D). The initial wavepacket (orange) splits in two wavepackets that propagate in opposite directions, towards the detector. c) Wavepacket dynamics in an M (left-handed) SnIP double-helix without spin-orbit interaction. Probability current for the CW (blue) and CCW (red) spinless wavepackets; the later multiplied by the factor -1 to improve clarity. b) Time-dependent electronic population in the detector, without the $j_{s,s'}^{SO}$ term.

Before we consider the spin-dependent transport, it is instructive to start by considering the spinless situation, in which case H_{SO} is disregarded. The results are presented in Figure 2, where panel c) shows the probability current for the CW (blue) and CCW (red) wavepackets as a function of time and panel d) shows the time-dependent electronic population in the detector, as given by the LHS and the RHS of Eq. (S33), without the $\mathbf{j}_{s,s'}^{SO}$ term. These results can be summarized as follows: 1) there is no observable difference for spinless wavepackets travelling along CW or CCW directions on M (Figure 2-c) or P-SnIP (Figure S2) strands; 2) the continuity equation derived for the TB formalism is consistent with the

quantum dynamics calculations (Figure 2-d); 3) the time-of-flight the wavepackets take to travel 45 unit cells (≈ 35.7 nm) in the absence of SOC is $\tau_{tof} = 109$ fs; and 4) by equating the LHS with RHS of Eq. (S33) we obtain a tight-binding effective mass of $m^* \approx 0.42 m_e$, which is similar to the value of $0.28 m_e$ that was obtained from ab-initio band structure calculations.³⁵ Thus, ignoring the SOC, the results for M-SnIP and P-SnIP strands show no observable difference (Figure S2).

In the remainder, we look into the effects caused by the interplay of the spin-orbit coupling with the chirality of the strands. Let us consider, for the sake of the argument, an initial state $\Psi(0) = \Psi_s$ in the source segment, with pure spin state $s_z = +1$ parallel to the \hat{z} axis of the M-SnIP double-helix. For practical reasons, we define the usage: $\{M(-),P(+)\}$ for designating the SnIP axial chirality, $\{CW,CCW\}$ for the wave propagation direction and $s=\{\uparrow,\downarrow\}$ for spin orientation parallel or anti-parallel to the \hat{z} axis. The spin-helicity of the propagating wavepacket is given by $h = \mathbf{S} \cdot \mathbf{v}/(|\mathbf{S}||\mathbf{v}|) \equiv \pm 1$, where \mathbf{S} is the spin vector and \mathbf{v} is the propagation velocity of the wavepacket, independently of the chirality of the strand. According to this definition, the CW wavepacket has **initially** $h_{cw}^\uparrow = +1$ whereas the CCW one has $h_{ccw}^\uparrow = -1$, so that $\hat{\mathcal{PT}}h_{cw}^\uparrow = h_{cw}^\downarrow = -h_{cw}^\uparrow$. Applying the time-reversal operation on the initial wavepackets we get the Kramers doublets: $\{h_{cw}^\uparrow, h_{ccw}^\downarrow\} = +1$ and $\{h_{ccw}^\uparrow, h_{cw}^\downarrow\} = -1$. In a free (achiral) medium, the dynamics of the wavepackets belonging to either of the doublets is equal, such as in the case of a beam of circularly polarized light propagating in an achiral medium. However, we ought to incorporate the chirality of the medium in the description. To do so, we define the parity-even symmetry index $\eta = Ch \equiv \pm 1$, where C stands for $\{M(-),P(+)\}$. It combines the spin-helicity of the electron with the chirality of the medium, rendering for the initial wavepackets $\eta_{cw}^{M\uparrow} = -1$ and $\eta_{ccw}^{M\uparrow} = +1$. By classifying the η index with respect to the \mathcal{PT} symmetries we get $\hat{\mathcal{PT}}\eta_{cw}^{M\uparrow} = \eta_{cw}^{P\downarrow} = -1$, and $\hat{\mathcal{PT}}\eta_{ccw}^{M\uparrow} = \eta_{ccw}^{P\downarrow} = +1$, and so on. Thus, considering all possible scenarios, *i.e.* the forward and backward propagating states of both spin orientations on helical strands of M and P chirality, the Kramers doublet is augmented to give rise to a fourfold doublet with $\{\eta_{cw}^{M\uparrow}, \eta_{ccw}^{M\downarrow}, \eta_{cw}^{P\downarrow}, \eta_{ccw}^{P\uparrow}\} \equiv \eta^-$ and $\{\eta_{ccw}^{M\uparrow}, \eta_{cw}^{M\downarrow}, \eta_{ccw}^{P\downarrow}, \eta_{cw}^{P\uparrow}\} \equiv \eta^+$.

After these general considerations, we now analyse the transport properties of electrons in a chiral SnIP strand taking into account the SO interaction. Figure S3-a shows that the probability current due to the wavepacket $\eta_{cw}^{M\uparrow} = -1$ is faster and has higher fluence rate than that of the counter-propagating wavepacket with $\eta_{ccw}^{M\uparrow} = 1$. The same behavior is

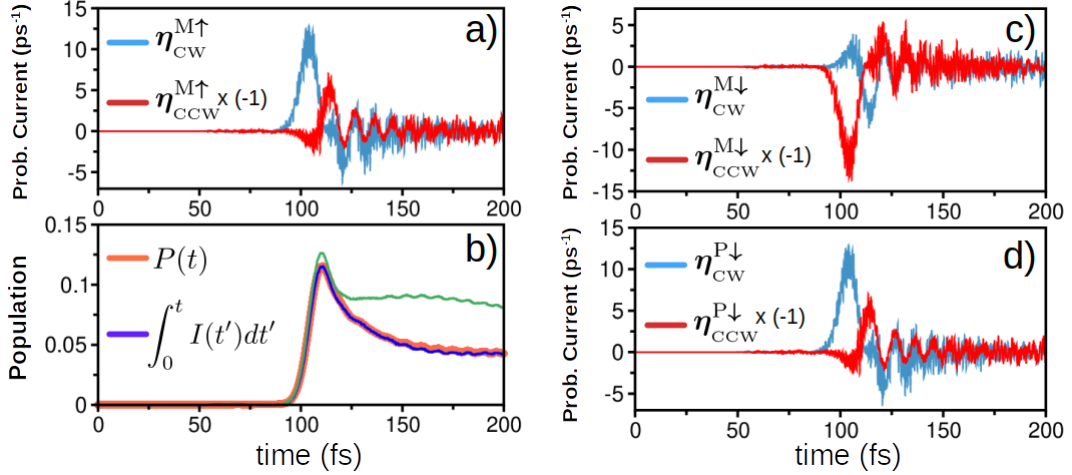


FIG. 3. a) Probability density currents at the detector segment D produced by the counter-propagating wavepackets revealing the asymmetry of propagation velocity. Probability current for the $\eta_{\text{cw}}^{M\uparrow} = \eta^-$ (blue) and $\eta_{\text{ccw}}^{M\uparrow} = \eta^+$ (red) wavepackets, the later multiplied by the -1 factor for the sake of clarity. Note that $v(\eta_{\text{cw}}^{M\uparrow}) > v(\eta_{\text{ccw}}^{M\uparrow})$. b) Time-dependent electronic population in the detector, as given by the LHS (orange) and the RHS (blue) terms of Eq. (S33). The green curve, obtained without the $\mathbf{j}_{s,s'}^{SO}$ term, evinces the relevance of the spin-mixed component of \mathbf{j} . Results for different counter-propagating wavepackets: c) $v(\eta_{\text{ccw}}^{M\downarrow}) > v(\eta_{\text{cw}}^{M\downarrow})$ and d) $v(\eta_{\text{cw}}^{P\downarrow}) > v(\eta_{\text{ccw}}^{P\downarrow})$. Note that $v(\eta_{\text{ccw}}^{M\downarrow}) = v(\eta_{\text{cw}}^{P\downarrow})$.

evinced for the probability current of the $\eta_{\text{cw,ccw}}^{M\downarrow}$ pair of contra-propagating wavepackets (Figure S3-c) and also for the $\eta_{\text{cw,ccw}}^{P\downarrow}$ pair (Figure S3-d). The consistency of the asymmetric propagation effect with the continuity equation is evinced in Figure S3-b, by the agreement between the time-dependent population (orange curve) with the probability density flux integrated over time (blue curve). It is also interesting to realize the relevance of $\mathbf{j}_{s,s'}^{SO}$ for the continuity equation, as revealed by the green curve in Figure S3-b that describes the time-integrated probability density flux without the spin-mixed term.

However, spin is not a paramount cause of the effect. In fact, a propagation velocity asymmetry has also been reported for electrons in SWCNT, neglecting altogether the spin-orbit interaction, but considering instead the orbital angular momentum of the carriers associated with the K and K' valleys. In this case the effect is produced by a curvature-induced effective spin-orbit interaction, and it is revealed after second order perturbation treatment. In a theoretical study Izumida et al.⁸ showed that left- and right-propagating

electrons in the same K (or K') valley have different velocities in chiral and armchair nanotubes. It was shown that $v_L^{(K)} > v_R^{(K)}$ but $v_R^{(K)} = v_L^{(K')}$, which can be mapped onto our results if $K(K') \iff \uparrow(\downarrow)$ and $L(R) \iff CW(CCW)$, so that $v(\eta_{CW}^{M\uparrow}) > v(\eta_{CCW}^{M\uparrow})$ but $v(\eta_{CW}^{M\uparrow}) = v(\eta_{CCW}^{M\downarrow})$. In general we have $v(\eta^-) > v(\eta^+)$ for the elements of the previously defined fourfold Kramers doublet. Yet another analogous phenomenon is the so called planar chirality effect,³⁴ whereby the transmission of circularly polarized EM waves through a planar chiral structure undergoes asymmetric propagation depending on the direction of wave propagation; note that the handedness of a planar chiral structure is reversed when observed from opposite sides of the structure's plane.

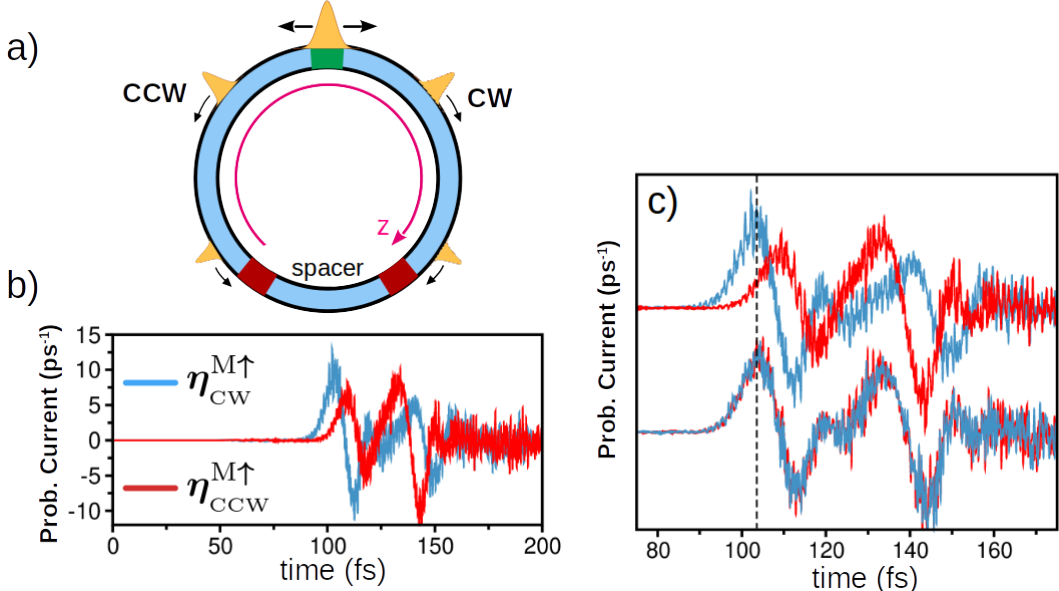


FIG. 4. a) Periodic M-SnIP double-helix. Two detector segments are considered, designated D_{CCW} and D_{CW} , separated by a spacer of length equal to 79.34 Å. b) Probability current for the $\eta_{CW}^{M\uparrow} = -1$ (blue) and $\eta_{CCW}^{M\uparrow} = +1$ (red) wavepackets. The time-of-flight is $\tau_{tof}(\eta_{CW}^{M\uparrow}) \approx 103$ fs and $\tau_{tof}(\eta_{CCW}^{M\uparrow}) \approx 109$ fs. c) Comparison between the spin-dependent (shifted up) and the spinless (shifted down) propagation dynamics, evincing that $v(\eta^-) \approx v_0$, where v_0 corresponds to the spinless case.

The ring structure of Figure 2 is not well suited to determine the propagation velocities of the counter-propagating wavepackets. Thus, we modified its structure to accommodate two detector segments, D_{CCW} and D_{CW} , both with the same size as the original D , but separated by a spacer segment of length 79.34 Å (shown in Figure 4-a). The distance between the

source (S) and the detectors (D_{CW} and D_{CCW}) is preserved (35.7 nm) as in the original structure. Then, we apply the continuity equation, Eq. (S33), to both detectors to evaluate the probability flux due to the counter propagating wavepackets (Figure 4-b). The positive peaks indicate the inflow of charge in the detector whereas the negative peaks are associated with the outflow. The time-of-flight for each case is $\tau_{tof} \approx 103$ fs for the $\eta_{CW}^{M\uparrow}$ wavepacket and $\tau_{tof} \approx 109$ fs for the $\eta_{CCW}^{M\uparrow}$ wavepacket, with the later being approximately 6% slower. Panel c) of Figure 4 compares the spin-dependent to the spinless propagation dynamics for this setup. We notice that $v(\eta^-) \approx v_0$, where v_0 corresponds to the spinless case, whereas $v(\eta^+)$ decreases, so that we have $v(\eta^-) \approx v_0 > v(\eta^+)$. Additional simulations performed for different ring setups (Figure S7) and different elements of the Kramers doublets corroborate the effect.

Discussions. We have shown that the mobility of electrons in structures with axial chirality depends on 3 factors, as described by the η index: the direction of the spin angular momentum (or for that matter an axial vector), the direction of motion and the chirality of the underlying structure, the three of them combined through a spin-orbit like interaction. As a result, we have $v(\eta^-) > v(\eta^+)$, as previously described, in qualitative agreement with the CISS phenomena.¹² Due to its generality, this effect should occur in a variety of systems that satisfy the aforementioned basic conditions. Scattering and decoherence perturbations, though, not taken into consideration in the present unitary quantum description, should also interfere with the measured effect. The environmental coupling (including defects and the vibrational normal modes of the structure) shall decrease considerably the coherence length of the electron. However, the spin polarization lifetime exceeds the transport time by several orders of magnitude. Thus, the spin-dependent quantum mobilities of the left- and right-propagating electrons in the chiral structure provide the basis for employing semiclassical frameworks, like the kinetic Monte Carlo method, to calculate the CISS effect in general situations. Another issue, not yet resolved, concerns the importance of the strength of the SO interaction. In SnIP, the elements Sn and I have strong intrinsic SOC constants, unlike the organic elements. However, for organic systems, the effective SO hamiltonian may be augmented by external electric fields due, for instance, to hydrogen bonds²⁵ or the influence of strain in the SO coupling.^{7,46} Yet another possibility is that the CISS effect has a nonlinear dependence on the SOC strength, evidenced perhaps in tunnel/hopping models.²⁷

Finally, once separation and stabilization of the SnIP enantiomers is attained, this ma-

terial could also be envisaged as a gyrotropic metamaterial in the form of thin films or coating, for it has recently been demonstrated that 3D-chiral metamaterials with strong chirality can exhibit unconventional optical properties such as negative refractive index and enhanced optical activity, among others.^{34,47,48}

Conclusions. In summary, based on general quantum mechanical principles we have derived a spin-current continuity equation using the tight-binding formalism, and showed its consistency with quantum dynamics calculations. The formalism was applied to the promising double-helix system SnIP. We derived an expression for the spin-mixed current and showed its importance for the spin conservation in spin transport experiments. Finally we have demonstrated the chirality induced propagation velocity asymmetry effect for charge transport in chiral systems and analysed its relevance to the chiral-induced spin selectivity (CISS) and other phenomena.

Acknowledgements. This study was financed by Coordenação de Aperfeiçoamento de Pessoal de Nível Superior Brasil (CAPES) - Finance Code 001, by the Brazilian National Counsel of Technological and Scientific Development (CNPq) and the National Institute for Organic Electronics (INEO). L.G.C.R. acknowledges allocation of supercomputer time from Laboratory for Scientific Computing (LNCC/MCTI, Brazil).

¹ L. D. Barron, J. Am. Chem. Soc. **108**, 5539 (1986).

² G. H. Wagnière, “Front matter,” in *On Chirality and the Universal Asymmetry* (John Wiley & Sons, Ltd, 2007).

³ R. Prange, M. Cage, K. Klitzing, S. Girvin, A. Chang, F. Duncan, M. Haldane, R. Laughlin, A. Pruisken, and D. Thouless, *The Quantum Hall Effect*, Graduate Texts in Contemporary Physics (Springer New York, 2012).

⁴ R. Saito, G. Dresselhaus, and M. S. Dresselhaus, *Physical Properties of Carbon Nanotubes* (Published by ImperiaL College Press and Distributed by World Scientific Publishing CO., 1998).

⁵ C. L. Kane and E. J. Mele, Phys. Rev. Lett. **78**, 1932 (1997).

⁶ T. Ando, J. Phys. Soc. Jpn. **69**, 1757 (2000).

⁷ D. Huertas-Hernando, F. Guinea, and A. Brataas, Phys. Rev. B **74**, 155426 (2006).

⁸ W. Izumida, A. Vikström, and R. Saito, *Phys. Rev. B* **85**, 165430 (2012).

⁹ J. W. G. Wilder, L. C. Venema, A. G. Rinzler, R. E. Smalley, and C. Dekker, *Nature* **391**, 59 (1998).

¹⁰ J. D. Watson and F. H. C. Crick, *Nature* **171**, 737 (1953).

¹¹ K. Ray, S. P. Ananthavel, D. H. Waldeck, and R. Naaman, *Science* **283**, 814 (1999).

¹² B. Göhler, V. Hamelbeck, T. Z. Markus, M. Kettner, G. F. Hanne, Z. Vager, R. Naaman, and H. Zacharias, *Science* **331**, 894 (2011).

¹³ R. Naaman, Y. Paltiel, and D. H. Waldeck, *Nat. Rev. Chem.* **3**, 250 (2019).

¹⁴ K. Banerjee-Ghosh, O. Ben Dor, F. Tassinari, E. Capua, S. Yochelis, A. Capua, S.-H. Yang, S. S. P. Parkin, S. Sarkar, L. Kronik, L. T. Baczewski, R. Naaman, and Y. Paltiel, *Science* **360**, 1331 (2018).

¹⁵ A. C. Aragonès, E. Medina, M. Ferrer-Huerta, N. Gimeno, M. Teixidó, J. L. Palma, N. Tao, J. M. Ugalde, E. Giralt, I. Díez-Pérez, and V. Mujica, *Small* **13**, 1602519 (2017).

¹⁶ S. Ghosh, S. Mishra, E. Avigad, B. P. Bloom, L. T. Baczewski, S. Yochelis, Y. Paltiel, R. Naaman, and D. H. Waldeck, *J. Phys. Chem. Lett.* **11**, 1550 (2020).

¹⁷ Y.-H. Kim, Y. Zhai, H. Lu, X. Pan, C. Xiao, E. A. Gaulding, S. P. Harvey, J. J. Berry, Z. V. Vardeny, J. M. Luther, and M. C. Beard, *Science* **371**, 1129 (2021).

¹⁸ K. B. Ghosh, W. Zhang, F. Tassinari, Y. Mastai, O. Lidor-Shalev, R. Naaman, P. Möllers, D. Nürenberg, H. Zacharias, J. Wei, E. Wierzbinski, and D. H. Waldeck, *J. Phys. Chem. C* **123**, 3024 (2019).

¹⁹ S. Ghosh, B. P. Bloom, Y. Lu, D. Lamont, and D. H. Waldeck, *J. Phys. Chem. C* **124**, 22610 (2020).

²⁰ R. Gutierrez, E. Díaz, C. Gaul, T. Brumme, F. Domínguez-Adame, and G. Cuniberti, *J. Phys. Chem. C* **117**, 22276 (2013).

²¹ M. Geyer, R. Gutierrez, V. Mujica, and G. Cuniberti, *J. Phys. Chem. C* **123**, 27230 (2019).

²² A.-M. Guo and Q.-F. Sun, *P. Natl. Acad. Sci. USA* **111**, 11658 (2014).

²³ S. Dalum and P. Hedegård, *Nano Lett.* **19**, 5253 (2019).

²⁴ M. S. Zöllner, S. Varela, E. Medina, V. Mujica, and C. Herrmann, *J. Chem. Theory Comput.* **16**, 2914 (2020).

²⁵ S. Varela, B. Montañes, F. López, B. Berche, B. Guillot, V. Mujica, and E. Medina, *J. Chem. Phys.* **151**, 125102 (2019).

²⁶ V. V. Maslyuk, R. Gutierrez, A. Dianat, V. Mujica, and G. Cuniberti, *J. Phys. Chem. Lett.* **9**, 5453 (2018).

²⁷ S. Varela, I. Zambrano, B. Berche, V. Mujica, and E. Medina, *Phys. Rev. B* **101**, 241410 (2020).

²⁸ X. Yang, C. H. van der Wal, and B. J. van Wees, *Phys. Rev. B* **99**, 024418 (2019).

²⁹ X. Yang, C. H. van der Wal, and B. J. van Wees, *Nano Lett.* **20**, 6148 (2020).

³⁰ A.-M. Guo and Q.-f. Sun, *Phys. Rev. Lett.* **108**, 218102 (2012).

³¹ S. Matityahu, Y. Utsumi, A. Aharony, O. Entin-Wohlman, and C. A. Balseiro, *Phys. Rev. B* **93**, 075407 (2016).

³² D. Pfister, K. Schäfer, C. Ott, B. Gerke, R. Pöttgen, O. Janka, M. Baumgartner, A. Efimova, A. Hohmann, P. Schmidt, S. Venkatachalam, L. van Wüllen, U. Schürmann, L. Kienle, V. Duppel, E. Parzinger, B. Miller, J. Becker, A. Holleitner, R. Weihrich, and T. Nilges, *Adv. Mat.* **28**, 9783 (2016).

³³ C. Ott, F. Reiter, M. Baumgartner, M. Pielmeier, A. Vogel, P. Walke, S. Burger, M. Ehrenreich, G. Kieslich, D. Daisenberger, J. Armstrong, U. K. Thakur, P. Kumar, S. Chen, D. Donadio, L. S. Walter, R. T. Weitz, K. Shankar, and T. Nilges, *Adv. Funct. Mat.* **29**, 1900233 (2019).

³⁴ V. A. Fedotov, P. L. Mladyonov, S. L. Prosvirnin, A. V. Rogacheva, Y. Chen, and N. I. Zheludev, *Phys. Rev. Lett.* **97**, 167401 (2006).

³⁵ D. N. Purschke, M. R. P. Pielmeier, E. Üzer, C. Ott, C. Jensen, A. Degg, A. Vogel, N. Amer, T. Nilges, and F. A. Hegmann, *Adv. Mat.* , 2100978.

³⁶ M. Baumgartner, R. Weihrich, and T. Nilges, *Chem.-Eur. J.* **23**, 6452 (2017).

³⁷ S. Varela, V. Mujica, and E. Medina, *Phys. Rev. B* **93**, 155436 (2016).

³⁸ D. Kienle, J. I. Cerdá, and A. W. Ghosh, *J. Appl. Phys.* **100**, 043714 (2006).

³⁹ F. Rostamzadeh Renani and G. Kirczenow, *Phys. Rev. B* **85**, 245415 (2012).

⁴⁰ W. H. Moores, R. McWeeny, and C. A. Coulson, *P. Roy. Soc. Lond. A Mat.* **332**, 365 (1973).

⁴¹ O. Ayed, E. Bernard, and B. Silvi, *J. Mol. Struc.-THEOCHEM* **135**, 159 (1986).

⁴² J. Shi, P. Zhang, D. Xiao, and Q. Niu, *Phys. Rev. Lett.* **96**, 076604 (2006).

⁴³ Q.-f. Sun and X. C. Xie, *Phys. Rev. B* **72**, 245305 (2005).

⁴⁴ N. Sasao, H. Okada, Y. Utsumi, O. Entin-Wohlman, and A. Aharony, *J. Phys. Soc. Jpn.* **88**, 064702 (2019).

⁴⁵ W. B. Hodge, S. V. Migirditch, and W. C. Kerr, *Am. J. Phys.* **82**, 681 (2014).

⁴⁶ F. Guinea, M. I. Katsnelson, and A. K. Geim, *Nat. Phys.* **6**, 30 (2010).

⁴⁷ E. Plum, J. Zhou, J. Dong, V. A. Fedotov, T. Koschny, C. M. Soukoulis, and N. I. Zheludev, Phys. Rev. B **79**, 035407 (2009).

⁴⁸ S. Zhang, Y.-S. Park, J. Li, X. Lu, W. Zhang, and X. Zhang, Phys. Rev. Lett. **102**, 023901 (2009).

⁴⁹ F. Rostamzadeh Renani and G. Kirczenow, Phys. Rev. B **87**, 121403 (2013).

⁵⁰ J. H. Ammeter, H. B. Buergi, J. C. Thibeault, and R. Hoffmann, J. Am. Chem. Soc. **100**, 3686 (1978).

⁵¹ D. A. Papaconstantopoulos and M. J. Mehl, J. Phys.-Condens. Mat. **15**, R413 (2003).

⁵² E. Condon, E. Condon, G. Shortley, H. B. P. C. of the History of Quantum Mechanics, and the Theory of Relativity, *The Theory of Atomic Spectra*, Cambridge Univ. Pr. 209 (Cambridge University Press, 1935).

⁵³ L. Cusachs and H. Aldrich, Chem. Phys. Lett. **12**, 197 (1971).

⁵⁴ W. C. Martin, J. Res. Natl. Bur. Stand.-A. Physics and Chemistry **75A**, 109 (1970).

⁵⁵ S. Küfner, J. Furthmüller, L. Matthes, M. Fitzner, and F. Bechstedt, Phys. Rev. B **87**, 235307 (2013).

⁵⁶ K. Dulitz, E. Bommeli, G. Grassi, D. Zindel, and F. Merkt, Mol. Phys. **114**, 2848 (2016).

⁵⁷ K. Rüdenberg, J. Chem. Phys. **19**, 1433 (1951).

Supporting Information for

Chirality Induced Propagation Velocity Asymmetry

I. TIGHT-BINDING HAMILTONIAN

We compute the tight-binding (TB) hamiltonian in the basis of atomic Slater-type orbitals (STO's), $|\chi_{nlm}s\rangle$, where $i = \{nlm\}$ represents the orbital quantum numbers associated with the wavefunction $\chi_{nlm}(\mathbf{r}_\alpha) = \mathcal{R}_n(r_\alpha)Y_m^l(\theta, \varphi)$, and $s = \{-1, 1\}$ (lowercase s) designates the spin state of the electron along the z direction. In particular, the wavefunction components $\mathcal{R}_n(r_\alpha)$ and $Y_m^l(\theta, \varphi)$ describe, respectively, the radial and angular parts of the STO for an atom located at position \mathbf{R}_α , with $\mathbf{r}_\alpha = \mathbf{r} - \mathbf{R}_\alpha$,

$$\langle \mathbf{r}_\alpha | n \rangle = \sqrt{\frac{2\zeta}{(2n)!}} (2\zeta)^n r_\alpha^{n-1} e^{-\zeta r_\alpha} Y_m^l(\theta, \varphi). \quad (\text{S1})$$

The basis set includes the 3s and 3p atomic orbitals for the phosphorus (P) atoms and the 5s and 5p orbitals for the tin (Sn) and iodine (I) atoms. Several studies have used the TB method, either in the Slater-Koster^{S7,S21,S23,S37} (SK) or the extended-Hückel^{S38,S39,S49} (eH) framework, to describe carbon nanotubes, DNA molecules and nanosystems alike. We adopt the extended-Hückel approach.

The total hamiltonian is comprised of a spinless part and the spin-orbit interaction part. The matrix elements of the spinless semiempirical extended-Hückel hamiltonian are defined as $H_{ij} = \kappa_{ij}S_{ij}$, where $\kappa_{ij} = K_{ij}(\varepsilon_i + \varepsilon_j)/2$ and $S_{ij}(\alpha, \beta) = \langle \chi_i(\mathbf{r}_\alpha) | \chi_j(\mathbf{r}_\beta) \rangle$ is the overlap between atomic orbitals i and j located at \mathbf{R}_α and \mathbf{R}_β , respectively, with $S_{ij} = \delta_{ij}$ when $\alpha = \beta$. The empirical parameters ε_i are generally associated with the negative ionization energies of the valence atomic orbitals and the parameter K_{ij} is the Wolfsberg–Helmholz empirical constant. We implement the modified Wolfsberg–Helmholz formula,^{S50} $K_{ij} = \bar{k}_{ij} + \Delta^2 + \Delta^4(1 - \bar{k}_{ij})$, with $\bar{k}_{ij} = (k_{\text{WH},i} + k_{\text{WH},j})/2$ and $\Delta = (\varepsilon_i - \varepsilon_j) / (\varepsilon_i + \varepsilon_j)$. The STO parameters used in this work are shown in Table I.

The total hamiltonian can be divided into a spinless part (H_0), associated with the eH-TB hamiltonian, and a spin-orbit (SO) interaction part

$$H_{SO} = \frac{1}{2(mc)^2} \mathbf{S} \cdot \nabla V(\mathbf{r}) \times \mathbf{p}, \quad (\text{S2})$$

where $\mathbf{S} = \frac{\hbar}{2}\boldsymbol{\sigma} = \frac{\hbar}{2}(\sigma_x, \sigma_y, \sigma_z)$ is the spin vector operator comprised of the σ Pauli matrices, $\mathbf{p} = -i\hbar\nabla$ is the electron momentum operator and $V(\mathbf{r})$ is the total Coulomb potential

energy felt by the electron. We follow the approach of Renani and Kirzcenow^{S39,S49} to write the spin-orbit hamiltonian in the framework of the eH-TB formalism. Despite the complexity of the SO operator, the main contribution of the SO interaction arises from the one-electron operators that couple the electron with the nuclei.^{S40} Therefore, in the TB method, the total Coulomb potential can be approximated by a summation over spherically symmetric single particle potentials produced by all the nuclei α , $V(\mathbf{r}) \approx \sum_{\alpha} V_{\alpha}(|\mathbf{r} - \mathbf{R}_{\alpha}|)$,^{S51} so that

$$H_{SO} \approx \sum_{\alpha} \frac{1}{2m^2c^2} \frac{1}{|\mathbf{r}_{\alpha}|} \frac{dV_{\alpha}(r_{\alpha})}{dr_{\alpha}} \mathbf{S} \cdot \mathbf{L}_{\alpha} = \sum_{\alpha} \hat{\lambda}_{\alpha}(r_{\alpha}) \frac{\mathbf{S} \cdot \mathbf{L}_{\alpha}}{\hbar^2}, \quad (S3)$$

with $\mathbf{L}_{\alpha} = (\mathbf{r} - \mathbf{R}_{\alpha}) \times \mathbf{p}$ describing the angular momentum of the electron with respect to atom α . It has been shown that the effective single particle SO operator $\xi_{\alpha} \mathbf{S} \cdot \mathbf{L}_{\alpha}$ produces very good results^{S40} when the coupling parameter ξ_{α} is obtained from ab-initio calculations or experimental fits, so as to incorporate SO many-body effects.

In the following, we make use of the transformation relations between the cubic harmonics (default in TB representation) and the spherical harmonics. The matrix elements of H_{SO} can be written as

$$\langle is_i, \beta | H_{SO} | js_j, \gamma \rangle = \sum_{\alpha} \langle is_i, \beta | \left(\hat{\lambda}_{\alpha}(r_{\alpha}) \frac{\mathbf{S} \cdot \mathbf{L}_{\alpha}}{\hbar^2} \right) | js_j, \gamma \rangle, \quad (S4)$$

with β and γ designating the atoms located at positions \mathbf{R}_{β} and \mathbf{R}_{γ} , which have orbital quantum numbers $i \equiv \{n_i l_i m_i\}$ and $j \equiv \{n_j l_j m_j\}$, respectively, as well as spin states s_i and s_j . The matrix element of Eq. (S4) renders *intra* and *inter*-atomic terms. Among them, the one-center *intra*-atomic terms ($\alpha = \beta = \gamma$) have overwhelming weight, followed by the two-center terms, for which two of the atomic site indices are equal, that account for 2% to 5% of the SO splitting.^{S40} The three-center terms ($\alpha \neq \beta \neq \gamma$) are, thus, disregarded altogether. Therefore, we have

$$\begin{aligned} \langle is_i, \beta | H_{SO} | js_j, \gamma \rangle &= \delta_{\beta, \gamma} \sum_{\alpha} \langle is_i, \beta | \left(\hat{\lambda}_{\alpha}(r_{\alpha}) \frac{\mathbf{S} \cdot \mathbf{L}_{\alpha}}{\hbar^2} \right) | js_j, \beta \rangle \\ &\quad + (1 - \delta_{\beta, \gamma}) \left[\langle is_i, \beta | \left(\hat{\lambda}_{\beta}(r_{\beta}) \frac{\mathbf{S} \cdot \mathbf{L}_{\beta}}{\hbar^2} \right) | js_j, \gamma \rangle + \langle is_i, \beta | \left(\hat{\lambda}_{\gamma}(r_{\gamma}) \frac{\mathbf{S} \cdot \mathbf{L}_{\gamma}}{\hbar^2} \right) | js_j, \gamma \rangle \right]. \end{aligned} \quad (S5)$$

We start by writing down the *intra*-atomic matrix element centered in atom α . Due to the spherical symmetry, the *intra*-atomic matrix elements can be factored as

$$\begin{aligned} \langle is_i | H_{SO}^{intra} | js_j \rangle_{\alpha} &= \langle is_i, \alpha | \hat{\lambda}_{\alpha}(r_{\alpha}) \frac{\mathbf{S} \cdot \mathbf{L}_{\alpha}}{\hbar^2} | js_j, \alpha \rangle \\ &= \langle \mathcal{R}(r_{\alpha}) | \hat{\lambda}_{\alpha}(r_{\alpha}) | \mathcal{R}(r_{\alpha}) \rangle \langle l_i m_i s_i, \alpha | \frac{\mathbf{S} \cdot \mathbf{L}_{\alpha}}{\hbar^2} | l_j m_j s_j, \alpha \rangle. \end{aligned} \quad (S6)$$

The angular part of Eq. (S6) preserves L_α and S , so that it is non-zero only for $l_i = l_j$,^{S52}

$$\begin{aligned} \langle l_i m_i s_i, \alpha | \mathbf{S} \cdot \mathbf{L}_\alpha | l_j m_j s_j, \alpha \rangle &= \frac{\hbar^2}{2} s_i m_i \delta_{l_j, m_j, s_j}^{l_i, m_i, s_i} \\ &+ \frac{\hbar^2}{2} \sqrt{l_j(l_j + 1) - m_j(m_j + s_j)} (1 - \delta_{s_i, s_j}) \delta_{l_j, m_j + s_j}^{l_i, m_i}. \end{aligned} \quad (\text{S7})$$

The radial part of Eq. (S6) can be associated with the empirical λ_{SOC} parameter

$$\langle \mathcal{R}(r_\alpha) | \hat{\lambda}_\alpha(r_\alpha) | \mathcal{R}(r_\alpha) \rangle = \lambda_\alpha^{SOC}. \quad (\text{S8})$$

We obtain the parameters λ_α^{SOC} from the literature, as shown in Table II, for the P, Sn and I elements. Hund's rules are adopted.^{S52}

Therefore, by combining the results of Eq. (S7) and Eq. (S8), we get for the *intra*-atomic matrix elements

$$\langle i s_i | H_{SO}^{intra} | j s_j \rangle_\alpha = \frac{\lambda_\alpha^{SOC}}{2} \left\{ m_i s_i \delta_{i,j} + \sqrt{l_j(l_j + 1) - m_j(m_j + s_j)} (1 - \delta_{s_i, s_j}) \delta_{l_j, m_j + s_j}^{l_i, m_i} \right\}. \quad (\text{S9})$$

For the *inter*-atomic matrix elements of Eq. (S5) we have

$$\langle i s_i, \beta | H_{SO}^{inter} | j s_j, \gamma \rangle = \langle i s_i, \beta | \hat{\lambda}_\beta(r_\beta) \frac{\mathbf{S} \cdot \mathbf{L}_\beta}{\hbar^2} | j s_j, \gamma \rangle + \langle i s_i, \beta | \hat{\lambda}_\gamma(r_\gamma) \frac{\mathbf{S} \cdot \mathbf{L}_\gamma}{\hbar^2} | j s_j, \gamma \rangle, \quad (\text{S10})$$

with $\beta \neq \gamma$. Since the one-center terms are much larger than the two-center ones,^{S40} we can use the Mulliken-Rüdenberg approximation^{S41, S57} to simplify the two-center integrals in terms of one-center integrals. In addition to the size difference, the fact that the radial part of the SO interaction decays approximately as r_α^{-3} indicates that the SO interaction is localized in space. Now, to be consistent with the eH formalism and the valence-electron assumption, the summation is carried out over the orthonormal basis set $\{k\}$ comprised of valence orbitals associated with the atoms β and γ . Thus, we obtain for Eq. (S10)

$$\begin{aligned} \langle i s_i, \beta | H_{SO}^{inter} | j s_j, \gamma \rangle &= \sum_{k \in \beta} \langle i s_i, \beta | \hat{\lambda}_\beta(r_\beta) \frac{\mathbf{S} \cdot \mathbf{L}_\beta}{\hbar^2} | k s_k, \beta \rangle \langle k s_k, \beta | j s_j, \gamma \rangle \\ &+ \sum_{k \in \gamma} \langle i s_i, \beta | k s_k, \gamma \rangle \langle k s_k, \gamma | \hat{\lambda}_\gamma(r_\gamma) \frac{\mathbf{S} \cdot \mathbf{L}_\gamma}{\hbar^2} | j s_j, \gamma \rangle \\ &= \sum_{\substack{k \in \beta \\ s_k = s_j}} \langle i s_i, \beta | \hat{\lambda}_\beta(r_\beta) \frac{\mathbf{S} \cdot \mathbf{L}_\beta}{\hbar^2} | k s_k, \beta \rangle S_{kj}(\beta, \gamma) \\ &+ \sum_{\substack{k \in \gamma \\ s_i = s_k}} S_{ik}(\beta, \gamma) \langle k s_k, \gamma | \hat{\lambda}_\gamma(r_\gamma) \frac{\mathbf{S} \cdot \mathbf{L}_\gamma}{\hbar^2} | j s_j, \gamma \rangle. \end{aligned} \quad (\text{S11})$$

Then, substituting Eq. (S9) into Eq. (S11) we obtain for the two-center *inter*-atomic matrix elements

$$\langle is_i, \beta | H_{SO}^{inter} | js_j, \gamma \rangle = \sum_{\substack{k \in \beta \\ s_k = s_j \\ l_k = l_i}} S_{kj}(\beta, \gamma) \langle is_i | H_{SO}^{intra} | ks_k \rangle_{\beta} + \sum_{\substack{k \in \gamma \\ s_k = s_i \\ l_k = l_j}} S_{ik}(\beta, \gamma) \langle ks_k | H_{SO}^{intra} | js_j \rangle_{\gamma}. \quad (\text{S12})$$

Before concluding, we also use the Mulliken approximation in the *intra*-atomic two-center terms below

$$\langle is_i, \beta | \sum_{\alpha} \left(\hat{\lambda}_{\alpha}(r_{\alpha}) \frac{\mathbf{S} \cdot \mathbf{L}_{\alpha}}{\hbar^2} \right) | js_j, \beta \rangle = \sum_{\alpha} \sum_{k, l \in \alpha} S_{ik}(\beta, \alpha) S_{lj}(\alpha, \beta) \langle ks_k | H_{SO}^{intra} | ls_l \rangle_{\alpha}, \quad (\text{S13})$$

recalling that $S_{ij} = \delta_{ij}$ when $\alpha = \beta$.

Finally, substituting Eq. (S13) and Eq. (S12) into Eq. (S5), we obtain the expression for the matrix elements of spin-orbit interaction in the eH-TB framework

$$\begin{aligned} \langle is_i, \beta | H_{SO} | js_j, \gamma \rangle &= \delta_{\beta, \gamma} \sum_{\alpha} \sum_{k, l \in \alpha} S_{ik}(\mathbf{r}_{\beta}, \mathbf{r}_{\alpha}) S_{lj}(\mathbf{r}_{\alpha}, \mathbf{r}_{\beta}) \langle ks_k | H_{SO}^{intra} | ls_l \rangle_{\alpha} + \\ &\quad (1 - \delta_{\beta, \gamma}) \left\{ \sum_{k \in \beta} S_{kj}(\mathbf{r}_{\beta}, \mathbf{r}_{\gamma}) \langle is_i | H_{SO}^{intra} | ks_k \rangle_{\beta} + \sum_{k \in \gamma} S_{ik}(\mathbf{r}_{\beta}, \mathbf{r}_{\gamma}) \langle ks_k | H_{SO}^{intra} | js_j \rangle_{\gamma} \right\}. \end{aligned} \quad (\text{S14})$$

Notice that the overlap matrix is block diagonal in the Hilbert space of the spinor.

II. SPIN-DEPENDENT PROBABILITY CURRENT

To obtain the spin-dependent probability current, we start with the single-particle time-dependent Schrödinger equation (TDSE)

$$i\hbar \frac{\partial}{\partial t} \Psi(\mathbf{r}, t) = \left\{ -\frac{\hbar^2}{2m} \nabla^2 + V(\mathbf{r}) + \frac{1}{2(mc)^2} \mathbf{S} \cdot \nabla V \times \mathbf{p} \right\} \Psi(\mathbf{r}, t), \quad (\text{S15})$$

where $\mathbf{p} = -i\hbar \nabla$ is the linear momentum operator and \mathbf{S} is the spin operator in the basis of S_z eigenstates,

$$\mathbf{S} = \frac{\hbar}{2} \begin{bmatrix} \hat{\mathbf{z}} & \hat{\mathbf{x}} - i\hat{\mathbf{y}} \\ \hat{\mathbf{x}} + i\hat{\mathbf{y}} & -\hat{\mathbf{z}} \end{bmatrix}, \quad (\text{S16})$$

which acts on the spinor $\Psi(\mathbf{r}, t) = \sum_{s=\uparrow, \downarrow} \Psi_s(\mathbf{r}, t)$.

In the framework of the eH-TB formalism, we have

$$i\hbar \frac{\partial}{\partial t} \Psi(\mathbf{r}, t) = \{H_0 + H_{SO}\} \Psi(\mathbf{r}, t), \quad (\text{S17})$$

with H_0 representing the eH-TB hamiltonian and H_{SO} is given by Eq. (S14).

It has been pointed out that the conventional spin current, usually defined as $\mathbf{j}_s = \frac{\hbar}{m} \Im m [\Psi_s^* \nabla \Psi_s]$, or alternatively in terms of the operator $(1/2)(\hat{\mathbf{v}} \hat{\mathbf{S}} + \hat{\mathbf{S}} \hat{\mathbf{v}})$, is incomplete and unphysical under spin-flip hamiltonians.^{S42-S45} To obtain the expression for spin-dependent continuity equation we base our approach on the work of Hodge et al.^{S45} Starting with Eq. (S15), we multiply this equation by the complex conjugate of the wavefunction, $\Psi^*(\mathbf{r}, t)$. Then conjugate Eq. (S15) and multiply it by $\Psi(\mathbf{r}, t)$. Subtracting the two equations, we obtain

$$\begin{aligned} \sum_{s=\uparrow,\downarrow} \frac{\partial |\Psi_s|^2}{\partial t} = & - \sum_{s=\uparrow,\downarrow} \left\{ \nabla \cdot \frac{\hbar}{2im} (\Psi_s^* \nabla \Psi_s - \Psi_s \nabla \Psi_s^*) \right\} \\ & - \frac{1}{2m^2 c^2} \sum_{s,s'} [\Psi_s^* \mathbf{S}_{s,s'} \cdot \nabla V \times \nabla \Psi_{s'} + \Psi_s \mathbf{S}_{s,s'}^* \cdot \nabla V \times \nabla \Psi_{s'}^*] \end{aligned} \quad (\text{S18})$$

$$\begin{aligned} \sum_{s=\uparrow,\downarrow} \frac{\partial |\Psi_s|^2}{\partial t} = & -\nabla \cdot \left\{ \frac{\hbar}{m} \sum_{\sigma=\uparrow,\downarrow} \Im m [\Psi_{\sigma}^* \nabla \Psi_{\sigma}] \right\} \\ & + \frac{1}{2m^2 c^2} \sum_{s,s'} [\Psi_s^* \mathbf{S}_{s,s'} \cdot \nabla \Psi_{s'} + \Psi_{s'} \mathbf{S}_{s,s'} \nabla \cdot \Psi_s^*] \times \nabla V, \end{aligned} \quad (\text{S19})$$

where we have used the property $\mathbf{S}_{s,s'}^* = \mathbf{S}_{s',s}$. Using the vector identity $\mathbf{A} \cdot (\mathbf{B} \times \mathbf{C}) = \mathbf{B} \cdot (\mathbf{C} \times \mathbf{A})$ on the second term of the RHS of Eq. (S19) we get

$$\begin{aligned} \sum_{s=\uparrow,\downarrow} \frac{\partial |\Psi_s|^2}{\partial t} = & -\nabla \cdot \left\{ \frac{\hbar}{m} \sum_{\sigma=\uparrow,\downarrow} \Im m [\Psi_{\sigma}^* \nabla \Psi_{\sigma}] \right\} \\ & + \frac{1}{2m^2 c^2} \sum_{s,s'} \nabla (\Psi_s^* \Psi_{s'}) \cdot (\nabla V \times \mathbf{S}_{s,s'}) , \end{aligned} \quad (\text{S20})$$

and

$$\nabla (\Psi_s^* \Psi_{s'}) \cdot (\nabla V \times \mathbf{S}_{s,s'}) = \nabla \cdot (\Psi_s^* \Psi_{s'} \nabla V \times \mathbf{S}_{s,s'}) - \Psi_s^* \Psi_{s'} \nabla \cdot (\nabla V \times \mathbf{S}_{s,s'}) . \quad (\text{S21})$$

Then, by noting that $\nabla \cdot (\nabla V \times \mathbf{S}_{s,s'}) = \mathbf{S}_{s,s'} \cdot (\nabla \times \nabla V) - \nabla V \cdot (\nabla \times \mathbf{S}_{s,s'}) \equiv 0$ in Eq. (S21), the continuity equation for the probability density becomes^{S45}

$$\begin{aligned} \sum_{s=\uparrow,\downarrow} \frac{\partial |\Psi_s|^2}{\partial t} = & -\nabla \cdot \left\{ \frac{\hbar}{m} \sum_{s=\uparrow,\downarrow} \Im m [\Psi_s^* \nabla \Psi_s] \right\} \\ & - \nabla \cdot \left\{ \frac{1}{2(mc)^2} \sum_{s,s'} [\Psi_s^* \mathbf{S}_{s,s'} \Psi_{s'}] \times \nabla V \right\} , \end{aligned} \quad (\text{S22})$$

where we identify the conventional probability density current of well defined spin channel

$$\mathbf{j}_s = \frac{\hbar}{m} \Im m [\Psi_s^* \nabla \Psi_s] \quad (\text{S23})$$

and the spin-mixed probability density current that is due to the SO interaction

$$\sum_{s'} \mathbf{j}_{s,s'}^{SO} = \sum_{s'} \frac{1}{2(mc)^2} [\Psi_s^* \mathbf{S}_{s,s'} \Psi_{s'}] \times \nabla V(\mathbf{r}). \quad (\text{S24})$$

The later has been associated with the torque dipole density^{S42} or the angular spin current density.^{S43}

Equations (S23) and (S24) were derived for the continuum space representation, starting from the hamiltonian given in Eq. (S15). To be consistent with the TB formalism that is used to calculate the wavepacket dynamics, we need to use an effective mass m^* instead of the free electron mass m_e . In our calculations the internal consistency is obtained with $m^* = 0.42m_e$, as described in the main text of the paper.

Furthermore, in order to have consistency between the TB matrix element of Eq. (S6) and the spin-orbit hamiltonian of Eq. (S2) we assume that the SOC constant is given by a Coulomb potential that is generated by an effective charge Q'_α – to be determined ahead – for each of the atomic species in the double-helix. That is

$$\nabla V(\mathbf{r}) \approx \sum_{\alpha} \nabla V_{\alpha}(\mathbf{r} - \mathbf{R}_{\alpha}) \approx \sum_{\alpha} \frac{-e}{r_{\alpha}} \frac{d}{dr_{\alpha}} \left(\frac{Q'_\alpha}{r_{\alpha}} \right) \mathbf{r}_{\alpha}. \quad (\text{S25})$$

Therefore, Eq. (S24) becomes

$$\sum_{s,s'} \mathbf{j}_{s,s'}^{SO} \approx \frac{e}{2(mc)^2} \sum_{\alpha} \frac{Q'_\alpha}{r_{\alpha}^3} \left\{ \sum_{s,s'} [\Psi_s^* \mathbf{S}_{s,s'} \Psi_{s'}] \times \mathbf{r}_{\alpha} \right\}. \quad (\text{S26})$$

Using the definition of \mathbf{S} , as given in Eq. (S16), the term inside brackets can be expanded as

$$\begin{aligned} \sum_{s,s'} [\Psi_s^* \mathbf{S}_{s,s'} \Psi_{s'}] \times \mathbf{r}_{\alpha} = \\ \psi_{\uparrow}^* \psi_{\uparrow} (S_{\uparrow\uparrow} \times \mathbf{r}_{\alpha}) + \psi_{\uparrow}^* \psi_{\downarrow} (S_{\uparrow\downarrow} \times \mathbf{r}_{\alpha}) + \psi_{\downarrow}^* \psi_{\uparrow} (S_{\downarrow\uparrow} \times \mathbf{r}_{\alpha}) + \psi_{\downarrow}^* \psi_{\downarrow} (S_{\downarrow\downarrow} \times \mathbf{r}_{\alpha}) = \\ \frac{\hbar}{2} [\psi_{\uparrow}^* \psi_{\uparrow} (\hat{\mathbf{z}} \times \mathbf{r}_{\alpha}) + \psi_{\uparrow}^* \psi_{\downarrow} ((\hat{\mathbf{x}} - i\hat{\mathbf{y}}) \times \mathbf{r}_{\alpha}) + \psi_{\downarrow}^* \psi_{\uparrow} ((\hat{\mathbf{x}} + i\hat{\mathbf{y}}) \times \mathbf{r}_{\alpha}) - \psi_{\downarrow}^* \psi_{\downarrow} (\hat{\mathbf{z}} \times \mathbf{r}_{\alpha})] = \\ \frac{\hbar}{2} [(\psi_{\uparrow}^* \psi_{\uparrow} - \psi_{\downarrow}^* \psi_{\downarrow}) (\hat{\mathbf{z}} \times \mathbf{r}_{\alpha}) + 2\Re e(\psi_{\uparrow}^* \psi_{\downarrow}) \hat{\mathbf{x}} \times \mathbf{r}_{\alpha} + 2\Im m(\psi_{\uparrow}^* \psi_{\downarrow}) (\hat{\mathbf{y}} \times \mathbf{r}_{\alpha})]. \end{aligned} \quad (\text{S27})$$

Because the double-helix is aligned along the $\hat{\mathbf{z}}$ direction, we disregard the first term of Eq. (S27), since it yields a probability density current perpendicular to that direction. Thus, we remain with

$$\begin{aligned} \sum_{s,s'} [\Psi_s^* \mathbf{S}_{s,s'} \Psi_{s'}] \times \mathbf{r}_\alpha &= \frac{\hbar}{2} [2\Re e(\psi_\uparrow^* \psi_\downarrow)(\hat{\mathbf{x}} \times \mathbf{r}_\alpha) + 2\Im m(\psi_\uparrow^* \psi_\downarrow)(\hat{\mathbf{y}} \times \mathbf{r}_\alpha)] \\ &= \hbar [\Re e(\psi_\uparrow^* \psi_\downarrow)(y_\alpha \hat{\mathbf{z}} - z_\alpha \hat{\mathbf{y}}) + \Im m(\psi_\uparrow^* \psi_\downarrow)(z_\alpha \hat{\mathbf{x}} - x_\alpha \hat{\mathbf{z}})] . \end{aligned} \quad (\text{S28})$$

Disregarding, again, the terms perpendicular to the axis of the double-helix ($\hat{\mathbf{z}}$) we obtain for Eq. (S26)

$$\sum_{s,s'} \mathbf{j}_{s,s'}^{SO} \approx \frac{e\hbar}{2(m^*c)^2} \left(\Re e(\psi_\uparrow^* \psi_\downarrow) \sum_\alpha \frac{Q'_\alpha y_\alpha}{r_\alpha^3} - \Im m(\psi_\uparrow^* \psi_\downarrow) \sum_\alpha \frac{Q'_\alpha x_\alpha}{r_\alpha^3} \right) \hat{\mathbf{z}}. \quad (\text{S29})$$

Finally, it is necessary to determine the effective charges Q'_α within the eH-TB formalism. To do so we turn to Eq. (S8) and make use of the spin-orbit coupling parameters of Table II, so that

$$\langle \mathcal{R}_n(r_\alpha) | \frac{-e\hbar^2}{2(m^*c)^2} \frac{1}{r_\alpha} \frac{d}{dr_\alpha} \left(\frac{Q'_\alpha}{r_\alpha} \right) | \mathcal{R}_n(r_\alpha) \rangle = \lambda_\alpha^{SOC}, \quad (\text{S30})$$

where $\mathcal{R}_n(r_\alpha)$ is the radial part of the STO for an atom with principal quantum number n , located at position \mathbf{R}_α . The integral can be solved as

$$\begin{aligned} \langle \mathcal{R}_n(r_\alpha) | \frac{1}{|\mathbf{r} - \mathbf{R}_\alpha|^3} | \mathcal{R}_n(r_\alpha) \rangle &= \frac{(2\zeta_{l,\alpha})^{2n_\alpha+1}}{(2n_\alpha)!} \int_0^\infty \frac{|\mathbf{r} - \mathbf{R}_\alpha|^{2n_\alpha-2} e^{-2\zeta_{l,\alpha}|\mathbf{r} - \mathbf{R}_\alpha|}}{|\mathbf{r} - \mathbf{R}_\alpha|^3} r^2 dr \\ &= \frac{2\zeta_{l,\alpha}^3}{n_\alpha(n_\alpha-1)(2n_\alpha-1)}, \end{aligned} \quad (\text{S31})$$

for $n_\alpha > 1$, where $\zeta_{l,\alpha}$ is the orbital exponent of the STO with angular momentum l . Since the spin-orbit coupling vanishes for s orbitals, only angular momentum $l = 1$ is taken into consideration. Thus, the effective charges Q'_α are given by

$$Q'_\alpha = \lambda_\alpha^{SOC} \frac{(m^*c)^2}{e\hbar^2 \zeta_{l,\alpha}^3} n_\alpha(n_\alpha-1)(2n_\alpha-1). \quad (\text{S32})$$

To calculate the electronic transport in the double helix we integrate the continuity equation over a volume \mathcal{V} along the nanowire axis, as shown in Figure S1, and apply the divergence theorem to obtain

$$\frac{\partial}{\partial t} [P_\uparrow + P_\downarrow]_\mathcal{V} = - \sum_s \int_s j_{z,s} dA_\perp - \int_s \left[\sum_{s,s'} j_{s,s'}^{SO} \right]_z dA_\perp, \quad (\text{S33})$$

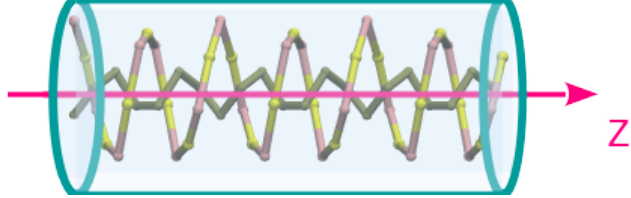


FIG. S1. Portion of the SnIP double-helix along the \hat{z} direction inside the boundary surface \mathcal{S} with inner volume \mathcal{V} .

where P_s is the spin-dependent electron population inside \mathcal{V} , associated with the spinor wavepackets $\Psi_s(\mathbf{r}, t)$. On the RHS, $j_{z,s}dA_{\perp}$ is the probability density flux with well defined spin projection across the surface caps perpendicular do the \hat{z} direction. The last term accounts for the probability density flux of the mixed-spin current.

III. SUPPORTING SIMULATION RESULTS

A. Spinless dynamics for M and P-SnIP

It is instructive to consider the spinless situation, when H_{SO} is disregarded. Panels a) and b), in Figure S2, show the wavepacket dynamics in an M (left-handed) SnIP double-helix, and panels c) and d) show the wavepacket dynamics in a P (right-handed) double-helix, both without SO interaction. There is no observable difference for spinless wavepackets travelling along CW or CCW directions on M or P-SnIP strands. The time-of-flight the wavepackets take to travel 45 unit cells (≈ 35.7 nm) in the absence of SOC is $\tau_{tof} = 109$ fs.

B. Spin-dependent dynamics for M and P-SnIP

Figures S3 to S5 describe the spin-dependent propagation dynamics for different combinations of the spin angular momentum, direction of motion, and chirality of the underlying physical structure.

TABLE I. Extended Hückel parameters used for the SnIP double-helix.

EHT-Symbol	N_{val}	n	spdf	ε_i (eV)	ζ(a₀⁻¹)	k_{WH}
P	5	3	s	-18.077	2.028	1.170
P	5	3	p	-14.016	2.160	2.872
Sn	4	5	s	-14.975	2.118	1.809
Sn	4	5	p	-8.186	2.159	2.452
I	7	5	s	-17.955	3.038	0.150
I	7	5	p	-13.190	2.426	2.571

 TABLE II. Intra-atomic spin-orbit coupling parameter. To obtain $λ_{SOC}$ for P an effective principal quantum number $n_{eff} = 1.51$ was used^{S53} in conjunction with the parameters of Martin^{S54}.

Element	$λ_{SOC}$ (eV)	$λ_{SOC}$ (cm ⁻¹)	Ref.
P	-0.00889	-71.7	Martin ^{S54}
Sn	0.68	5484.6	Küfner <i>et al.</i> ^{S55}
I	-0.62848	-5069.0	Dulitz <i>et al.</i> ^{S56}

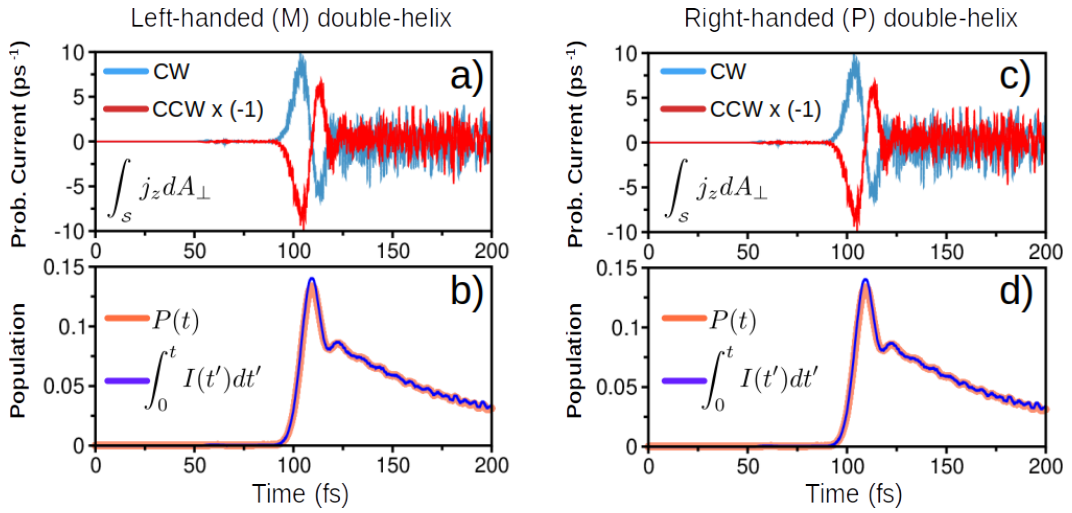


FIG. S2. Wavepacket dynamics in an M (left-handed) SnIP double-helix without spin-orbit interaction. a) Probability current for the CW (blue) and CCW (red) spinless wavepackets; the later multiplied by the factor -1 to improve clarity. b) Time-dependent electronic population in the detector volume \mathcal{V} , without the $j_{s,s'}^{SO}$ term. Analogous data for wavepacket dynamics in a P (right-handed) SnIP double-helix in panels c) and d). Ignoring the SOC, the propagation of spinless electrons for M-SnIP and P-SnIP strands are equal.

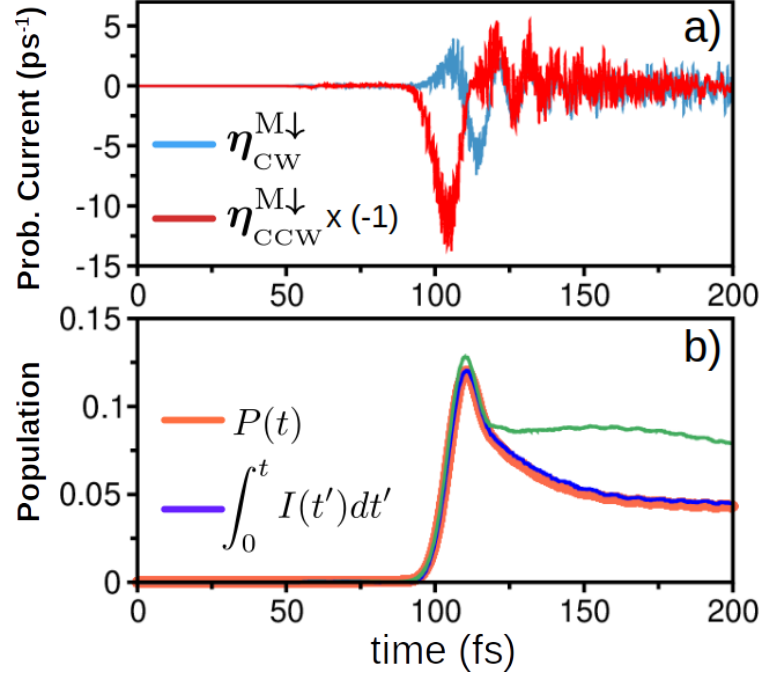


FIG. S3. a) Probability density currents at the detector segment D produced by the counter-propagating wavepackets revealing the asymmetry of propagation velocity. Probability current for the $\eta_{\text{CW}}^{M\downarrow} = \eta^+$ (blue) and $\eta_{\text{CCW}}^{M\downarrow} = \eta^-$ (red) wavepackets, the later multiplied by the -1 factor for the sake of clarity. Note that $v(\eta_{\text{CCW}}^{M\downarrow}) > v(\eta_{\text{CW}}^{M\downarrow})$. b) Time-dependent electronic population in the detector volume \mathcal{V} , as given by the LHS (orange) and the RHS (blue) terms of Eq. (19). The green curve, obtained without the $\mathbf{j}_{s,s'}^{\text{SO}}$ term, evinces the relevance of the spin-mixed component of \mathbf{j} .

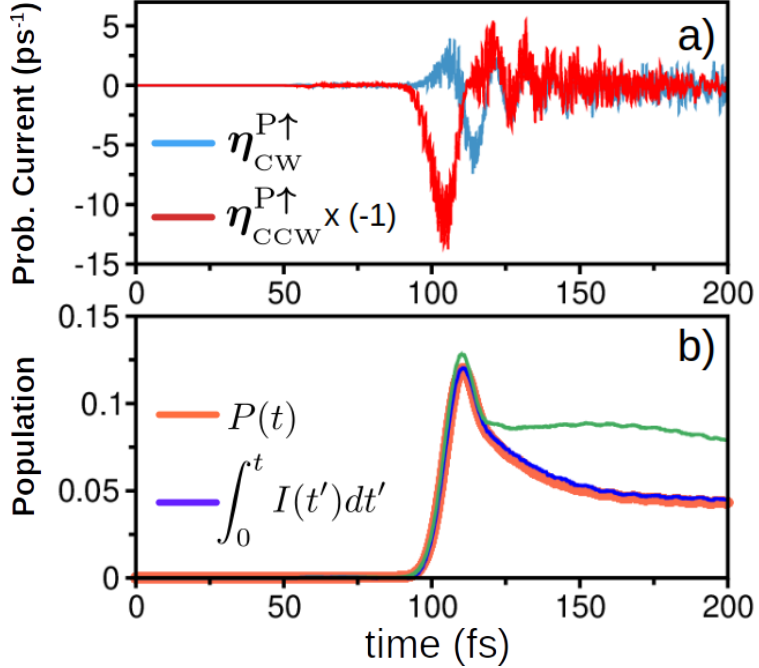


FIG. S4. a) Probability density currents at the detector segment D produced by the counter-propagating wavepackets revealing the asymmetry of propagation velocity. Probability current for the $\eta_{\text{CW}}^{\text{P}\uparrow} = \eta^+$ (blue) and $\eta_{\text{CCW}}^{\text{P}\uparrow} = \eta^-$ (red) wavepackets, the later multiplied by the -1 factor for the sake of clarity. Note that $v(\eta_{\text{CCW}}^{\text{P}\uparrow}) > v(\eta_{\text{CW}}^{\text{P}\uparrow})$. b) Time-dependent electronic population in the detector volume \mathcal{V} , as given by the LHS (orange) and the RHS (blue) terms of Eq. (19). The green curve, obtained without the $\mathbf{j}_{s,s}^{\text{SO}}$ term, evinces the relevance of the spin-mixed component of \mathbf{j} .

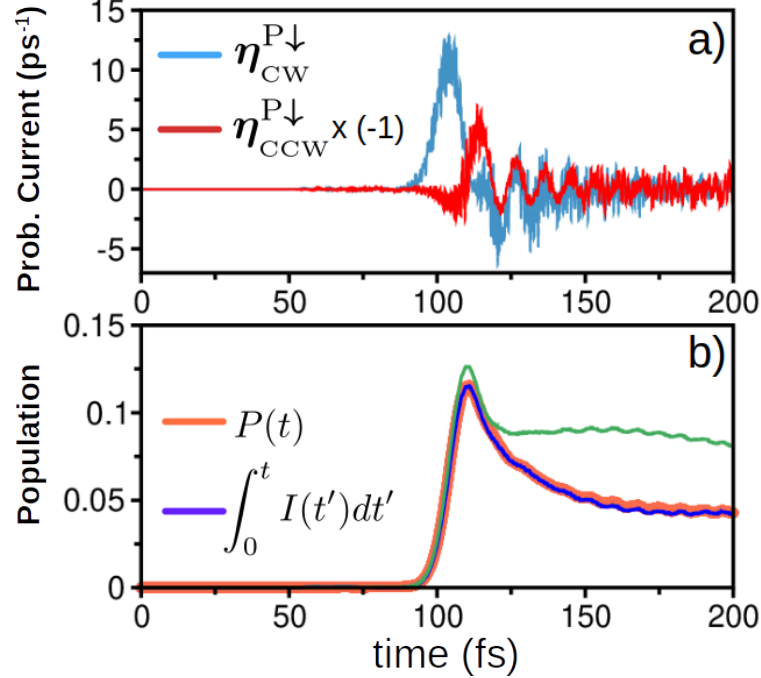


FIG. S5. a) Probability density currents at the detector segment D produced by the counter-propagating wavepackets revealing the asymmetry of propagation velocity. Probability current for the $\eta_{\text{CW}}^{\text{P}\downarrow} = \eta^-$ (blue) and $\eta_{\text{CCW}}^{\text{P}\downarrow} = \eta^+$ (red) wavepackets, the later multiplied by the -1 factor for the sake of clarity. Note that $v(\eta_{\text{CW}}^{\text{P}\downarrow}) > v(\eta_{\text{CCW}}^{\text{P}\downarrow})$. b) Time-dependent electronic population in the detector volume \mathcal{V} , as given by the LHS (orange) and the RHS (blue) terms of Eq. (19). The green curve, obtained without the $\mathbf{j}_{s,s'}^{\text{SO}}$ term, evinces the relevance of the spin-mixed component of \mathbf{j} .

C. Spin-dependent dynamics for different propagation lengths in the M-SnIP double helix

In relation to Figure S6, we consider the ring structure shown in Figure 4-a) of the paper, which is used to determine the propagation velocities of the CW and CCW wavepackets. The structure accommodates two detector segments, D_{CCW} and D_{CW} , both with the same size, but separated by a spacer segment of length 7.93 nm. The distance between the source (S) segment and each of the detectors (D_{CW} and D_{CCW}) is varied as: a) 7.9 nm (10 unit cells); b) 15.8 nm (20 unit cells); c) 23.8 nm (30 unit cells); and d) 31.7 nm (40 unit cells). Then, we apply the continuity equation, Eq. (S33), to both detectors to evaluate the probability flux due to the counter propagating wavepackets. The positive peaks indicate the inflow of charge in the detector whereas the negative peaks are associated with the outflow. Table III gives the time-of-flight for each case.

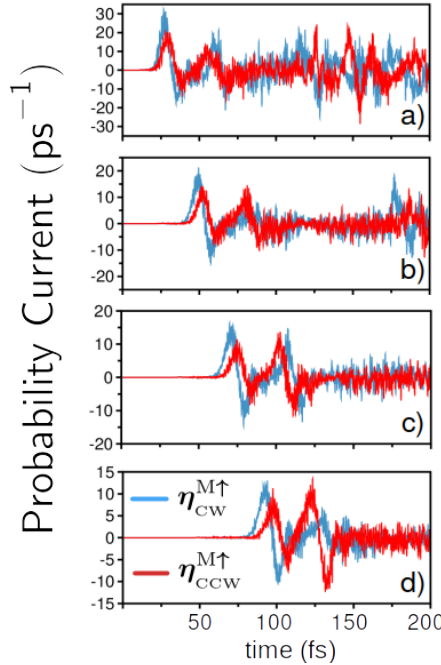


FIG. S6. Probability current for the $\eta_{CW}^{M\uparrow} = -1$ (blue) and $\eta_{CCW}^{M\uparrow} = +1$ (red) wavepackets, evincing the asymmetry of propagation velocities: $v(\eta_{CW}^{M\uparrow}) > v(\eta_{CCW}^{M\uparrow})$. The distance between the source (S) segment and each of the detectors (D_{CW} and D_{CCW}) is varied as: a) 7.9 nm (10 unit cells); b) 15.8 nm (20 unit cells); c) 23.8 nm (30 unit cells); and d) 31.7 nm (40 unit cells).

A linear fit to the data of Table III yields the ballistic propagation velocities $v(\eta^-) \approx$

TABLE III. Time-of-flight (τ_{tof}) as a functions of the distance between the source (S) segment and each of the detectors (D_{CW} and D_{CCW})

Distance between S and D segments	7.9 (nm)	15.8 (nm)	23.8 (nm)	31.7 (nm)	35.7 (nm)
τ_{tof} (fs) $\eta_{CW}^{M\uparrow} = \eta^-$	27	50	71	93	103
τ_{tof} (fs) $\eta_{CCW}^{M\uparrow} = \eta^+$	29	53	75	98	109

3.67 Å/fs and $v(\eta^+) \approx 3.48$ Å/fs

D. Comparison of Spinless and Spin-dependent dynamics

Figure S7 presents a comparison between the spinless dynamics (without SO interaction) and the spin-dependent dynamics (with SOI considered). For the sake of argument, we consider the M-SnIP double helix and the $\eta_{CW}^{M\uparrow} = -1$ (blue) and $\eta_{CCW}^{M\uparrow} = +1$ (red) wavepackets. For the spinless case we simply have the CW (blue) and CCW (red) wavepackets. For presentation purposes, the spin-dependent probability currents have been shifted up and those for the spinless case have been shifted down. The panels a), b), c) and d) correspond to different distances between the source (S) segment and each of the detectors (D_{CW} and D_{CCW}), namely: a) 7.9 nm (10 unit cells); b) 15.8 nm (20 unit cells); c) 23.8 nm (30 unit cells); and d) 31.7 nm (40 unit cells). Figure S7 shows that the propagation velocity $v(\eta^-) \approx v_0$, where v_0 corresponds to the spinless case, whereas $v(\eta^+)$ decreases, so that we have $v(\eta^-) \approx v_0 > v(\eta^+)$. Simulations performed on the other wavepackets that comprise the Kramers doublets revealed the same behaviour.

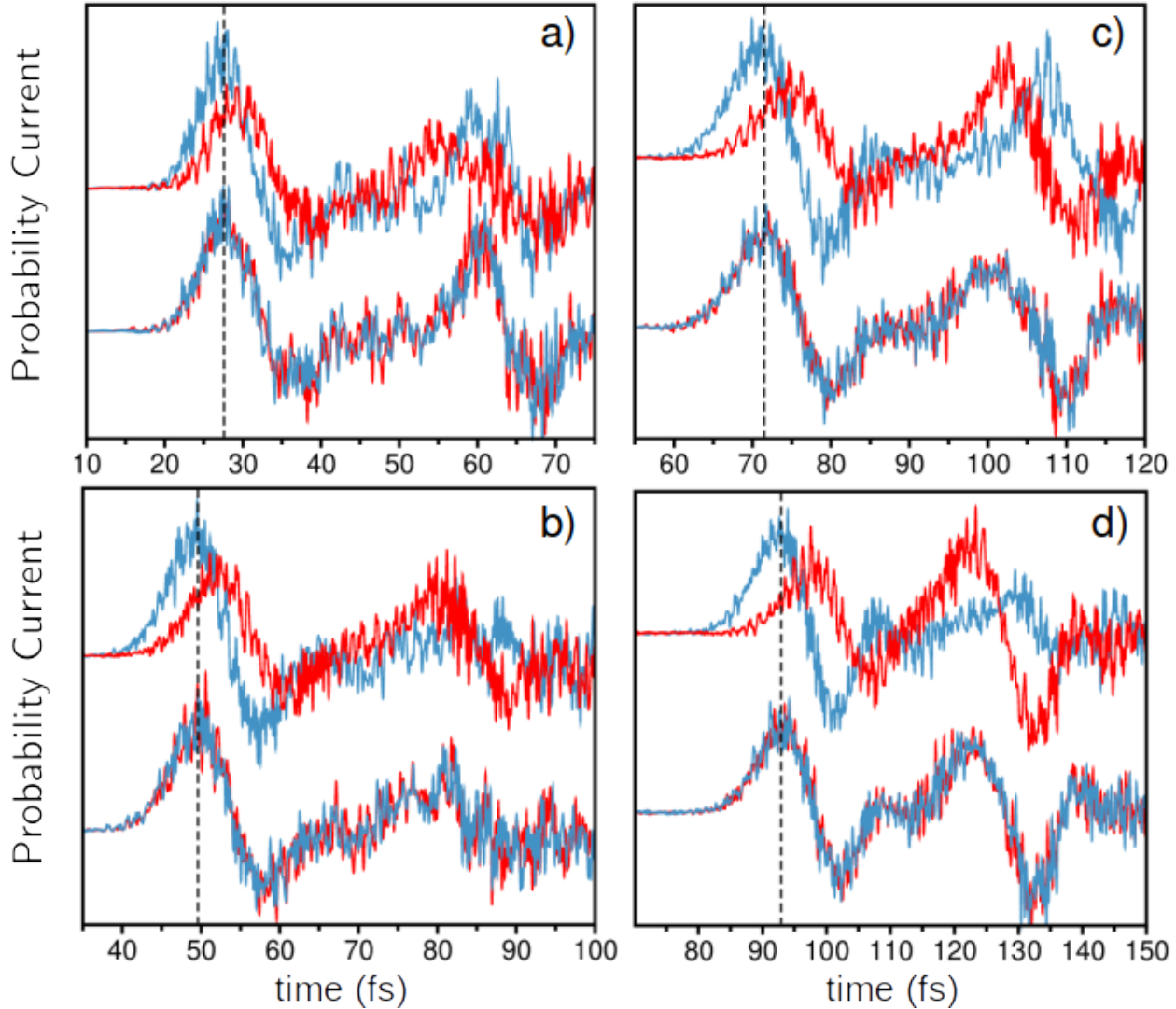


FIG. S7. Probability current for the $\eta_{CW}^{M\uparrow} = -1$ (blue) and $\eta_{CCW}^{M\uparrow} = +1$ (red) wavepackets, shifted up. Probability current for the CW (blue) and CCW (red) spinless wavepackets, shifted down. The distance between the source (S) segment and each of the detectors (D_{CW} and D_{CCW}) is varied as: a) 7.9 nm (10 unit cells); b) 15.8 nm (20 unit cells); c) 23.8 nm (30 unit cells); d) 31.7 nm (40 unit cells).

- [S1] L. D. Barron, *J. Am. Chem. Soc.* **108**, 5539 (1986).
- [S2] G. H. Wagnière, “Front matter,” in *On Chirality and the Universal Asymmetry* (John Wiley & Sons, Ltd, 2007).
- [S3] R. Prange, M. Cage, K. Klitzing, S. Girvin, A. Chang, F. Duncan, M. Haldane, R. Laughlin, A. Pruisken, and D. Thouless, *The Quantum Hall Effect*, Graduate Texts in Contemporary Physics (Springer New York, 2012).
- [S4] R. Saito, G. Dresselhaus, and M. S. Dresselhaus, *Physical Properties of Carbon Nanotubes* (Published by ImperiaL College Press and Distributed by World Scientific Publishing CO., 1998).
- [S5] C. L. Kane and E. J. Mele, *Phys. Rev. Lett.* **78**, 1932 (1997).
- [S6] T. Ando, *J. Phys. Soc. Jpn.* **69**, 1757 (2000).
- [S7] D. Huertas-Hernando, F. Guinea, and A. Brataas, *Phys. Rev. B* **74**, 155426 (2006).
- [S8] W. Izumida, A. Vikström, and R. Saito, *Phys. Rev. B* **85**, 165430 (2012).
- [S9] J. W. G. Wilder, L. C. Venema, A. G. Rinzler, R. E. Smalley, and C. Dekker, *Nature* **391**, 59 (1998).
- [S10] J. D. Watson and F. H. C. Crick, *Nature* **171**, 737 (1953).
- [S11] K. Ray, S. P. Ananthavel, D. H. Waldeck, and R. Naaman, *Science* **283**, 814 (1999).
- [S12] B. Göhler, V. Hamelbeck, T. Z. Markus, M. Kettner, G. F. Hanne, Z. Vager, R. Naaman, and H. Zacharias, *Science* **331**, 894 (2011).
- [S13] R. Naaman, Y. Paltiel, and D. H. Waldeck, *Nat. Rev. Chem.* **3**, 250 (2019).
- [S14] K. Banerjee-Ghosh, O. Ben Dor, F. Tassinari, E. Capua, S. Yochelis, A. Capua, S.-H. Yang, S. S. P. Parkin, S. Sarkar, L. Kronik, L. T. Baczewski, R. Naaman, and Y. Paltiel, *Science* **360**, 1331 (2018).
- [S15] A. C. Aragonès, E. Medina, M. Ferrer-Huerta, N. Gimeno, M. Teixidó, J. L. Palma, N. Tao, J. M. Ugalde, E. Giralt, I. Díez-Pérez, and V. Mujica, *Small* **13**, 1602519 (2017).
- [S16] S. Ghosh, S. Mishra, E. Avigad, B. P. Bloom, L. T. Baczewski, S. Yochelis, Y. Paltiel, R. Naaman, and D. H. Waldeck, *J. Phys. Chem. Lett.* **11**, 1550 (2020).
- [S17] Y.-H. Kim, Y. Zhai, H. Lu, X. Pan, C. Xiao, E. A. Gaulding, S. P. Harvey, J. J. Berry, Z. V. Vardeny, J. M. Luther, and M. C. Beard, *Science* **371**, 1129 (2021).

[S18] K. B. Ghosh, W. Zhang, F. Tassinari, Y. Mastai, O. Lidor-Shalev, R. Naaman, P. Möllers, D. Nürenberg, H. Zacharias, J. Wei, E. Wierzbinski, and D. H. Waldeck, *J. Phys. Chem. C* **123**, 3024 (2019).

[S19] S. Ghosh, B. P. Bloom, Y. Lu, D. Lamont, and D. H. Waldeck, *J. Phys. Chem. C* **124**, 22610 (2020).

[S20] R. Gutierrez, E. Díaz, C. Gaul, T. Brumme, F. Domínguez-Adame, and G. Cuniberti, *J. Phys. Chem. C* **117**, 22276 (2013).

[S21] M. Geyer, R. Gutierrez, V. Mujica, and G. Cuniberti, *J. Phys. Chem. C* **123**, 27230 (2019).

[S22] A.-M. Guo and Q.-F. Sun, *P. Natl. Acad. Sci. USA* **111**, 11658 (2014).

[S23] S. Dalum and P. Hedegård, *Nano Lett.* **19**, 5253 (2019).

[S24] M. S. Zöllner, S. Varela, E. Medina, V. Mujica, and C. Herrmann, *J. Chem. Theory Comput.* **16**, 2914 (2020).

[S25] S. Varela, B. Montañes, F. López, B. Berche, B. Guillot, V. Mujica, and E. Medina, *J. Chem. Phys.* **151**, 125102 (2019).

[S26] V. V. Maslyuk, R. Gutierrez, A. Dianat, V. Mujica, and G. Cuniberti, *J. Phys. Chem. Lett.* **9**, 5453 (2018).

[S27] S. Varela, I. Zambrano, B. Berche, V. Mujica, and E. Medina, *Phys. Rev. B* **101**, 241410 (2020).

[S28] X. Yang, C. H. van der Wal, and B. J. van Wees, *Phys. Rev. B* **99**, 024418 (2019).

[S29] X. Yang, C. H. van der Wal, and B. J. van Wees, *Nano Lett.* **20**, 6148 (2020).

[S30] A.-M. Guo and Q.-f. Sun, *Phys. Rev. Lett.* **108**, 218102 (2012).

[S31] S. Matityahu, Y. Utsumi, A. Aharony, O. Entin-Wohlman, and C. A. Balseiro, *Phys. Rev. B* **93**, 075407 (2016).

[S32] D. Pfister, K. Schäfer, C. Ott, B. Gerke, R. Pöttgen, O. Janka, M. Baumgartner, A. Efimova, A. Hohmann, P. Schmidt, S. Venkatachalam, L. van Wüllen, U. Schürmann, L. Kienle, V. Duppel, E. Parzinger, B. Miller, J. Becker, A. Holleitner, R. Weihrich, and T. Nilges, *Adv. Mat.* **28**, 9783 (2016).

[S33] C. Ott, F. Reiter, M. Baumgartner, M. Pielmeier, A. Vogel, P. Walke, S. Burger, M. Ehrenreich, G. Kieslich, D. Daisenberger, J. Armstrong, U. K. Thakur, P. Kumar, S. Chen, D. Donadio, L. S. Walter, R. T. Weitz, K. Shankar, and T. Nilges, *Adv. Funct. Mat.* **29**, 1900233 (2019).

[S34] V. A. Fedotov, P. L. Mladyonov, S. L. Prosvirnin, A. V. Rogacheva, Y. Chen, and N. I. Zheludev, Phys. Rev. Lett. **97**, 167401 (2006).

[S35] D. N. Purschke, M. R. P. Pielmeier, E. Üzer, C. Ott, C. Jensen, A. Degg, A. Vogel, N. Amer, T. Nilges, and F. A. Hegmann, Adv. Mat. , 2100978.

[S36] M. Baumgartner, R. Weihrich, and T. Nilges, Chem.-Eur. J. **23**, 6452 (2017).

[S37] S. Varela, V. Mujica, and E. Medina, Phys. Rev. B **93**, 155436 (2016).

[S38] D. Kienle, J. I. Cerdá, and A. W. Ghosh, J. Appl. Phys. **100**, 043714 (2006).

[S39] F. Rostamzadeh Renani and G. Kirczenow, Phys. Rev. B **85**, 245415 (2012).

[S40] W. H. Moores, R. McWeeny, and C. A. Coulson, P. Roy. Soc. Lond. A Mat. **332**, 365 (1973).

[S41] O. Ayed, E. Bernard, and B. Silvi, J. Mol. Struc.-THEOCHEM **135**, 159 (1986).

[S42] J. Shi, P. Zhang, D. Xiao, and Q. Niu, Phys. Rev. Lett. **96**, 076604 (2006).

[S43] Q.-f. Sun and X. C. Xie, Phys. Rev. B **72**, 245305 (2005).

[S44] N. Sasao, H. Okada, Y. Utsumi, O. Entin-Wohlman, and A. Aharony, J. Phys. Soc. Jpn. **88**, 064702 (2019).

[S45] W. B. Hodge, S. V. Migirditch, and W. C. Kerr, Am. J. Phys. **82**, 681 (2014).

[S46] F. Guinea, M. I. Katsnelson, and A. K. Geim, Nat. Phys. **6**, 30 (2010).

[S47] E. Plum, J. Zhou, J. Dong, V. A. Fedotov, T. Koschny, C. M. Soukoulis, and N. I. Zheludev, Phys. Rev. B **79**, 035407 (2009).

[S48] S. Zhang, Y.-S. Park, J. Li, X. Lu, W. Zhang, and X. Zhang, Phys. Rev. Lett. **102**, 023901 (2009).

[S49] F. Rostamzadeh Renani and G. Kirczenow, Phys. Rev. B **87**, 121403 (2013).

[S50] J. H. Ammeter, H. B. Buergi, J. C. Thibeault, and R. Hoffmann, J. Am. Chem. Soc. **100**, 3686 (1978).

[S51] D. A. Papaconstantopoulos and M. J. Mehl, J. Phys.-Condens. Mat. **15**, R413 (2003).

[S52] E. Condon, E. Condon, G. Shortley, H. B. P. C. of the History of Quantum Mechanics, and the Theory of Relativity, *The Theory of Atomic Spectra*, Cambridge Univ. Pr. 209 (Cambridge University Press, 1935).

[S53] L. Cusachs and H. Aldrich, Chem. Phys. Lett. **12**, 197 (1971).

[S54] W. C. Martin, J. Res. Natl. Bur. Stand.-A. Physics and Chemistry **75A**, 109 (1970).

[S55] S. Küfner, J. Furthmüller, L. Matthes, M. Fitzner, and F. Bechstedt, Phys. Rev. B **87**, 235307 (2013).

[S56] K. Dulitz, E. Bommeli, G. Grassi, D. Zindel, and F. Merkt, Mol. Phys. **114**, 2848 (2016).

[S57] K. Rüdenberg, J. Chem. Phys. **19**, 1433 (1951).